

A mechanism to control and detect rogue waves by plane wave initial conditions: the prototypical example of the damped and periodically driven NLS equation

Sevastos Diamantidis,¹ Theodoros P. Horikis,² and Nikos I. Karachalios¹

¹*Department of Mathematics, University of the Aegean, Karlovassi, GR 83200 Samos, Greece*

²*Department of Mathematics, University of Ioannina, Ioannina 45110, Greece*

Investigating by direct numerical simulations the dynamics of the damped and forced nonlinear Schrödinger equation in the presence of a time periodic forcing and for certain parametric regimes, we show that the wave-number of a plane-wave initial condition dictates the number of emerged Peregrine type rogue waves at the early stages of modulation instability. Another dynamical feature is that the formation of these events gives rise to the same number of transient “triangular” spatio-temporal patterns, each of which is reminiscent of the one emerging in the dynamics of the integrable NLS in its semi-classical limit, with vanishing initial conditions. The effects of the various parameters in modifying the above behavior are also discussed, and found to be far from its integrable limit counterpart. Furthermore, we find that the L^2 - norm of the spatial derivative and the L^4 -norm of the solution provide diagnostics for the time of appearance of rogue waves as local extrema in their evolution. This effect in the transient dynamics of the system is not detected by any of the standard conserved quantities of the integrable limit, while the long time dynamics are explained in terms of the global attractor possessed by the system and the asymptotic orbital stability of spatially uniform continuous wave solutions.

I. INTRODUCTION

Key element in the study of extreme events and rogue waves is predicting the location and time of their occurrence [1–4]. This is particularly difficult as the mechanisms that generate these waves are complex and highly nonlinear in nature. Furthermore, as modulation instability (MI) [5] is believed to be the main mechanism for their formation [6–8], another complication is added, as different initial states, under MI, will produce different events in both amplitude, and location.

It is argued and justified by numerous experimental observations, that in deep water and other physical systems like optics, plasmas [9–11] etc., the rogue wave dynamics are governed by the nonlinear Schrödinger (NLS) equation and its variants. The rogue wave events are modelled by the so-called Peregrine soliton [12], which is a rational solution of the NLS equation, in its integrable form [13].

However, when additional phenomena are added, such as viscosity, wind effects, opposing currents or higher order effects [14–21], the integrable NLS system is insufficient to describe the resulting dynamics. As such, additional, physically relevant terms, are incorporated in the model in order to account for these different effects. In this spirit, the present paper investigates once more, the wealth of the dynamics arising from the variant of the NLS equation with linear damping and a time-periodic forcing term:

$$iu_t + \frac{\nu}{2}u_{xx} + \sigma|u|^2u = -i\gamma u + \Gamma \exp(i\Omega t). \quad (1)$$

The parameter ν measures the second-order dispersion, σ the strength of the nonlinearity; both $\nu, \sigma > 0$ are motivated by the focusing integrable limit. The parameter $\gamma > 0$ is the strength of the linear damping (loss). The parameter $\Gamma > 0$ measures the amplitude of time-periodic forcing and $\Omega \in \mathbb{R}$ is its time frequency; subscripts denote partial derivatives. The model is of significance in numerous physical contexts, from nonlinear optics to plasma physics [22], and is one of the prototypical partial differential equations exhibiting complex spatiotemporal behavior [23–28].

It is further revealed that the simplest continuous wave (cw) initial condition

$$u(x, 0) = u_0(x) = A \exp\left(-\frac{iK\pi x}{L}\right), \quad (2)$$

when the system is supplemented with periodic boundary conditions in the fundamental interval $\mathcal{Q} = [-L, L]$,

$$u(-L, t) = u(L, t), \quad (3)$$

creates dynamical effects, which are –to our knowledge– novel and can be relevant to mechanisms for the detection/generation of rogue waves.

First, it may determine by its wave number K and for suitable amplitudes A , the emergence of an equal number of K Peregrine-type rogue waveforms at the initial stages of its evolution. By a comparison against the profile of the

analytical Peregrine rogue wave (PRW) of the integrable limit ($\gamma = \Gamma = 0$), it is judged that the profiles of these PRW-type waveforms do not only have similar profiles, but also share for a significant-time interval, growth and decay rates, remarkably close to that of the PRW of the integrable limit. A second new dynamical effect we identified, is the following: the PRW-type waveforms which emerge as first events in the dynamics are on the top of an equal number K of triangular-type (“Christmas tree”) spatiotemporal patterns [29]. Despite the fact that the initial condition does not decay at infinity, each one of these patterns possesses a structure similar to the single spatiotemporal pattern formed in the case of the integrable NLS, in its semi-classical limit [30–32].

Second, we discuss the potential structural robustness of the above dynamical behavior, as the several parameters of the system are varied, and we find that it persists up to certain threshold values for the parameters. We found that is far from the dynamics of the integrable limit as it is not observed in this limit when the same initial condition is posed.

Third, we find the following dynamical feature: the square of the L^2 -norm of the spatial derivative

$$D(t) = \int_{\mathcal{Q}} |u_x(x, t)|^2 dx, \quad (4)$$

and the L^4 -functional

$$\|u(t)\|_{L^4}^4 = \int_{\mathcal{Q}} |u(x, t)|^4 dx, \quad (5)$$

detect the emergence of the rogue waves as local extrema in their evolution in a time interval of enhanced instability, exactly at the time of their appearance. We found that only these functionals exhibit this detection property of extreme events as opposed to either of the standard conserved quantities of the integrable limit, namely the momentum,

$$M(t) = \text{Im} \int_{\mathcal{Q}} u(x, t) \overline{u_x}(x, t) dx, \quad (6)$$

the power (also called mass or wave action),

$$P(t) = \|u(t)\|_{L^2}^2 = \int_{\mathcal{Q}} |u(x, t)|^2 dx, \quad (7)$$

the Hamiltonian energy,

$$H(t) = \nu \int_{\mathcal{Q}} |u_x(x, t)|^2 dx - \sigma \int_{\mathcal{Q}} |u(x, t)|^4 dx. \quad (8)$$

The quantities (6)-(8) are three of the conserved quantities in an infinite hierarchy in the integrable case. In fact it was the conservation of the Hamiltonian energy of the integrable limit which motivated us to explain the detection from its parts $D(t)$ and $\|u(t)\|_{L^4}^4$ (this will become more clear later in the text). For $D(t)$, the manifestation of local extrema can be explained by the steep gradients of the Peregrine-type waveforms. For $\|u(t)\|_{L^4}^4$, the balance laws justify that it is suitably vertically translated above $D(t)$ at least for a finite time interval, explaining the detection of rogue waves at the same times.

Finally, the long-time asymptotics of the solutions, as observed by the involved functionals, are analytically justified in the parametric regimes we are interested in, by the global asymptotic orbital stability of cw solutions. The analytical arguments combine the linear stability analysis of spatially uniform, cw-solutions (see Theorem IV.1), with the well known results on the existence of a global attractor possessed by the associated infinite dimensional dynamical system and the notion of orbital stability (see Theorem IV.2). These arguments prove that the observed instabilities in the parametric regimes of rogue waves emergence are only transient in the presence of the orbital globally asymptotically stable cw-state. The results of relevant numerical experiments were found to be in excellent agreement with the analytical predictions.

The presentation of the paper is the following. In Section II, we report the numerical results on the observation of rogue-wave dynamics. In Section III we discuss the relevant balance laws of (1) for functionals, recall some useful estimates for our analysis and justify the functional type diagnostics for the detection of rogue-waves. In Section IV, we explain the asymptotic behavior of the solutions observed in terms of the orbital stability of spatially uniform cw solutions. The last Section IV, briefly discusses our conclusions and sketches a plan for future investigations.

II. NUMERICAL RESULTS

A. Emergence of extreme events and spatiotemporal patterns.

We start the presentation of the numerical results by discussing the spatiotemporal dynamics of the system, varying the wave number $K \geq 2$ of the initial condition (2), keeping its amplitude fixed, $A = 1$; the case $K = 1$ will be discussed at the end of Section IV.

Fig. 1 depicts the spatiotemporal evolution of the density $|u(x, t)|^2$ of the solution for various cases of the initial wave number $K \geq 2$. The parameters for Eq. (1) are $\nu = \sigma = 1$, $\gamma = 0.01$, $\Gamma = 0.1$, $\Omega = -2$ and $L = 50$.

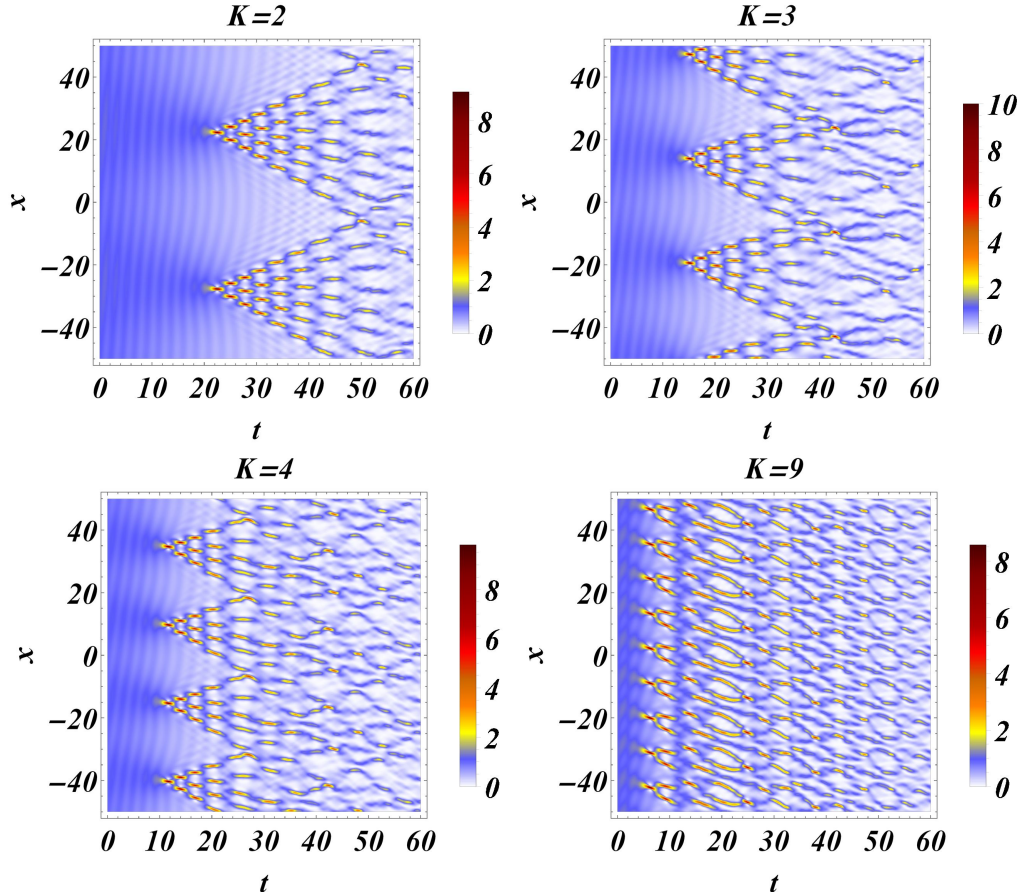


Figure 1: (Color Online) Dynamics of the cw-initial condition (2) for $A = 1$, varying its wavenumber K . The panels show the spatiotemporal evolution of the density $|u|^2$ for each K . Other parameters for the problem (1)-(3): $\nu = \sigma = 1$, $\gamma = 0.01$, $\Gamma = 0.1$, $\Omega = -2$ and $L = 50$.

Each one of the panels of Fig. 1 is associated with one of the snapshots portrayed in Fig. 2, showing the profiles of the first localized structures emerged in the contour plots of Fig. 2.

Combining the results presented in both figures, the following dynamical features are revealed:

1. The first events in the spatiotemporal dynamics (first “spots” observed in the contour plots of Fig. 1), correspond to localized waveforms possessing extreme amplitude (at least eight-times higher than the initial one). The initial wave number K gives rise to K -localized waveforms, which are formed on the top of a finite background, as shown in the snapshots of Fig. 2.
2. Subsequently, the dynamics are manifested by a formation of transient K -patterns with the following characteristics: each one is a distinct spatiotemporal region separated by nonlinear caustics which bound the pattern of the transient spatiotemporal oscillations. Particularly, a structured “lattice” of extreme events occurs, occupying a triangular region formed between the caustics. Progressively, their amplitude is decreasing, as we may conjecture due to the effect of damping. This is evident in the cases $K = 2, 3, 4$. Each of these patterns is

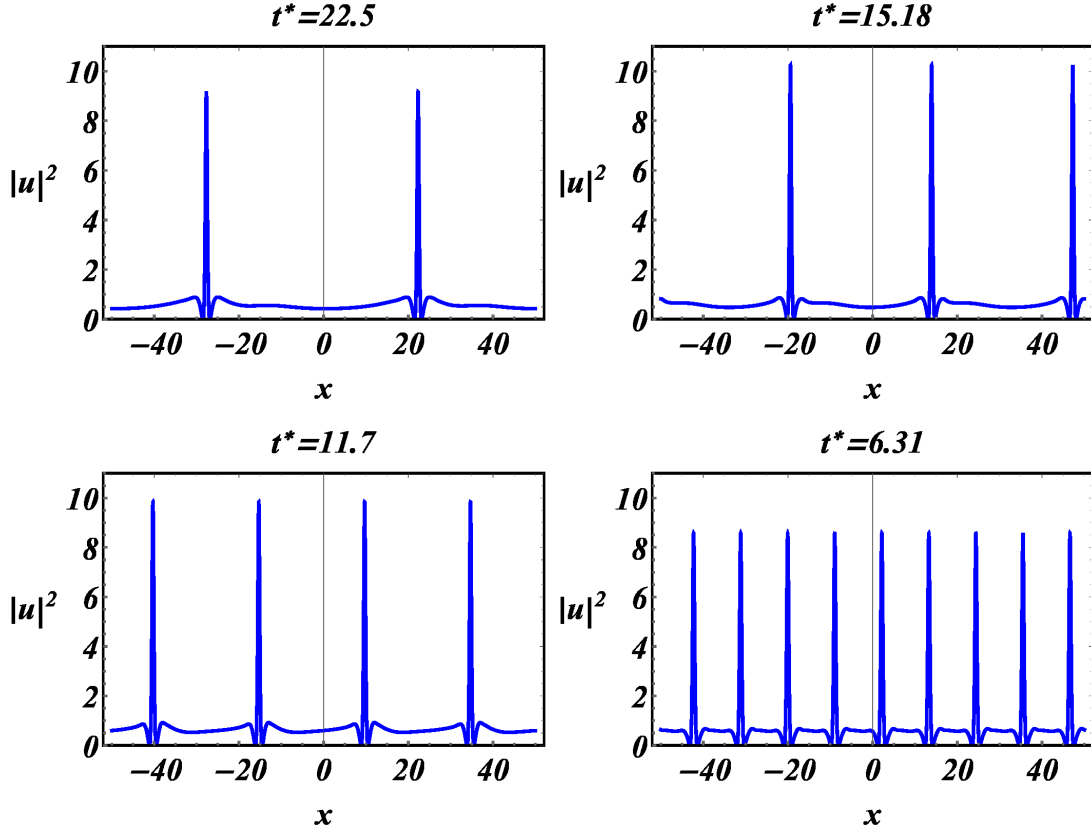


Figure 2: (Color Online) Snapshots of the density $|u|^2$ of the solution, at the times of the emergence of the PRW-type waveforms (first events in the dynamics). These correspond to the first events shown in the contour plots and the related parameter values of Fig. 1.

reminiscent of the pattern forming in the case of the integrable NLS *in its semiclassical limit*

$$i\epsilon u_t + \frac{\epsilon^2}{2} u_{xx} + |u|^2 u = 0, \quad (9)$$

for $\epsilon \rightarrow 0$ [30, 31], when supplemented with vanishing boundary conditions. We recall that in the case of the NLS (9), the single lattice in [30–32], is occupied by PRW structures defined by spots which correspond to the poles of the tritonquée solution of the Painlevé-I equation. A similar single pattern was also observed in the case of the damped and forced NLS for algebraically or exponentially vanishing initial data when the driver is spatiotemporally localized $\lim_{|x|^2+|t|^2 \rightarrow \infty} f(x, t) = 0$, [33], and explained in terms of decaying estimates in [34], but differs dramatically from the pattern observed in [35] in the dynamics of (1) initiated from the same vanishing initial conditions. Another interesting feature observed in our case, is that the points of intersection of the caustics are points of wave interference, occupied by localized structures of large amplitude.

3. The “area” occupied by the above “Christmas tree” patterns [29], is decreasing as the initial wave number is increasing; a compression of the triangular regions is observed in the case $K = 9$. However, this is only an effect of the increased excited modes against the fixed spatial region compressing the aforementioned pattern formation. This can be clarified further, when the numerical experiments for increased length L of the spatial interval and some large K are presented. The left panel of Fig. 3 shows the contour plot of the spatiotemporal evolution of the density when $K = 8$ and the same set of parameters as in Fig. 2, but for $L = 200$.

We clearly observe the formation of $K = 8$ -copies of the triangular pattern with the characteristics discussed above, as it is further clarified by the magnification offered in the right panel of Fig. 3 (showing two of them within the region $x \in [-50, 50]$, $t \in [0, 60]$). This study also reveals that the emergence of the above patterns is robust against variations with respect to the half-length L .

4. Do the first extreme events share characteristics of the PRW? To answer this question we shall implement fitting

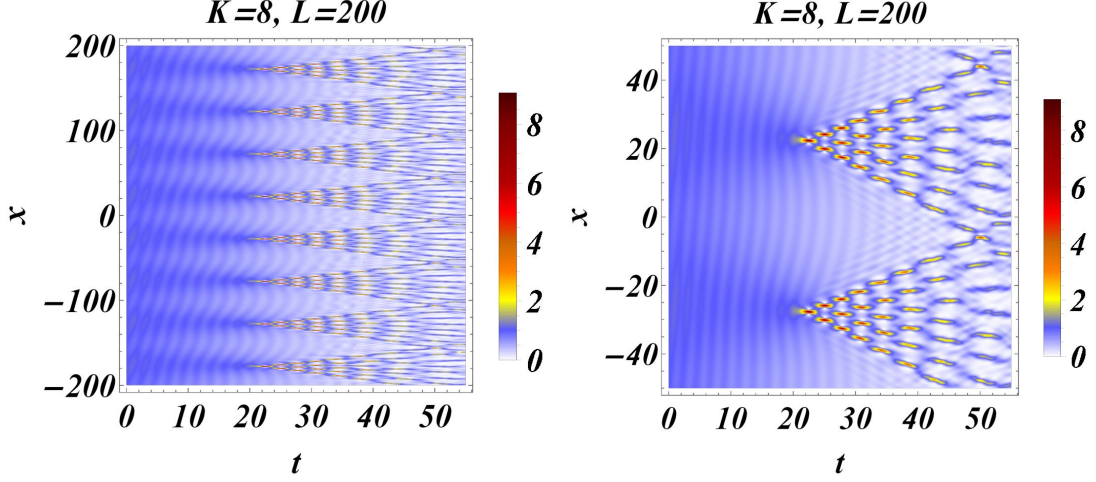


Figure 3: (Color Online) Dynamics of the cw-initial condition (2) for $A = 1$, $K = 8$, $L = 200$. The left panel shows the spatiotemporal evolution of the density for $x \in [-L, L]$ and $t \in [0, 60]$. The right panel offers a magnification of the patterns observed in the left panel, for $x \in [-50, 50]$ and $t \in [0, 60]$. Other parameters for the problem (1)-(3) are: $\nu = \sigma = 1$, $\gamma = 0.01$, $\Gamma = 0.1$, $\Omega = -2$.

arguments already used in [29, 35, 36], against the analytical PRW of the integrable NLS:

$$u_{\text{PS}}(x, t; P_0) = \sqrt{P_0} \left[1 - \frac{4 \left(1 + \frac{2it}{\Lambda} \right)}{1 + \frac{4x^2}{K_0^2} + \frac{4t^2}{\Lambda^2}} \right] \exp \left(\frac{it}{\Lambda} \right). \quad (10)$$

Recall that P_0 is the amplitude (power) of the continuous background supporting the PRW (10), and the parameters $\Lambda = \frac{1}{\sigma P_0}$, $K_0 = \sqrt{\nu \Lambda}$. We denote the space-time translations of (10) by $u_{\text{PS}}(x - x^*, t - t^*; P_0)$. The location x^* , time t^* and power P_0 , are numerically calculated: The power of its background P_0 is locked, so that the amplitude of the analytical PRW (10) coincides with the maximum amplitude of the extreme localized structures portrayed in 4 attained at time t^* . The position x^* is detected so that the center of the analytical PRW coincides with the center of a selected extreme event (from the group of the K -identical localized structures).

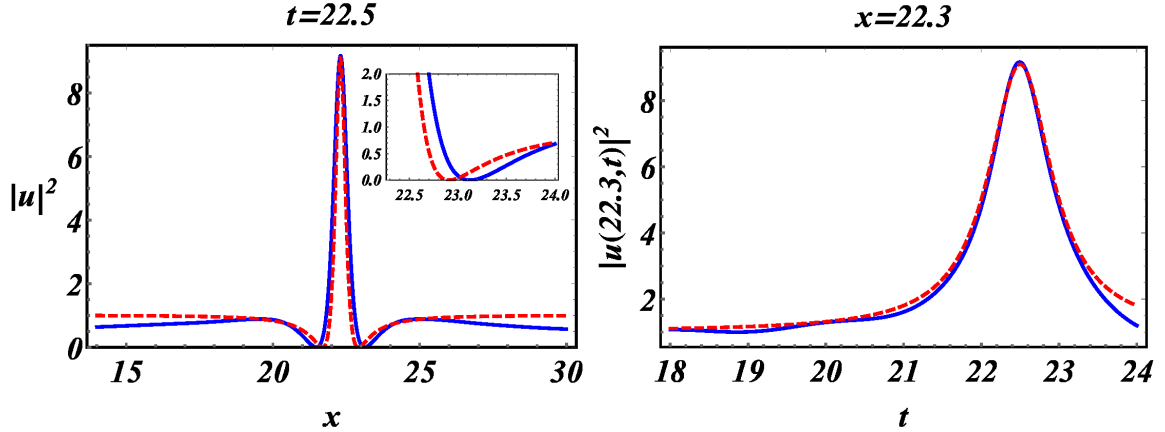


Figure 4: (Color Online) Comparison of the right PRW-type waveform observed in upper left panel of 1 [continuous (blue) curve], against the space-time translation of the analytical PRW of the integrable limit $u_{\text{PS}}(x - 22.3, t - 22.5; 1.01)$ where $K_0 = 0.70$ and $\Lambda = 0.99$ [dashed (red) curve]. The left panel compares the profiles. The right panel shows a comparison of the evolution of the density of their peaks $|u(22.3, t)|^2$ and $u_{\text{PS}}(0, t - 22.5; 1.01)$ respectively, for $t \in [18, 24]$.

The left panel of Fig. 4 justifies the similarity of the profile of the right extreme event of maximum amplitude attained at $t^* = 22.5$ [continuous (blue) curve] to the profile of the PRW $u_{\text{PS}}(x - 22.3, t - 22.5; 1.01)$, with $K_0 = 0.70$ and $\Lambda = 0.99$. The inset shows a detail around the left of the symmetric minima; the slopes of

the two curves show that the extreme event for the damped and forced NLS should possess, around the core, a spatial decay rate close to that of the PRW. The right panel of Fig. 4 depicts the comparison of the evolution of the density of the centers of the two waves; their time growth is very close for $t \in [18, 21]$, their coincidence becomes almost exact for $t \in [21.5, 23.5]$ and afterwards we observe their divergence. Thus, the emerged waves for the damped and forced model possess for significant time intervals the algebraic in time, growth and decay rate of a PRW.

5. *Dynamics of the integrable limit $\gamma = \Gamma = 0$.* The above “Christmas tree” pattern formation is not exhibited in the integrable limit but only in the damped and forced case of (1), for certain parametric regimes (see below). This is verified in Fig. 5 showing the spatiotemporal dynamics in this limit and for the rest of parameters fixed as in Fig. 1.

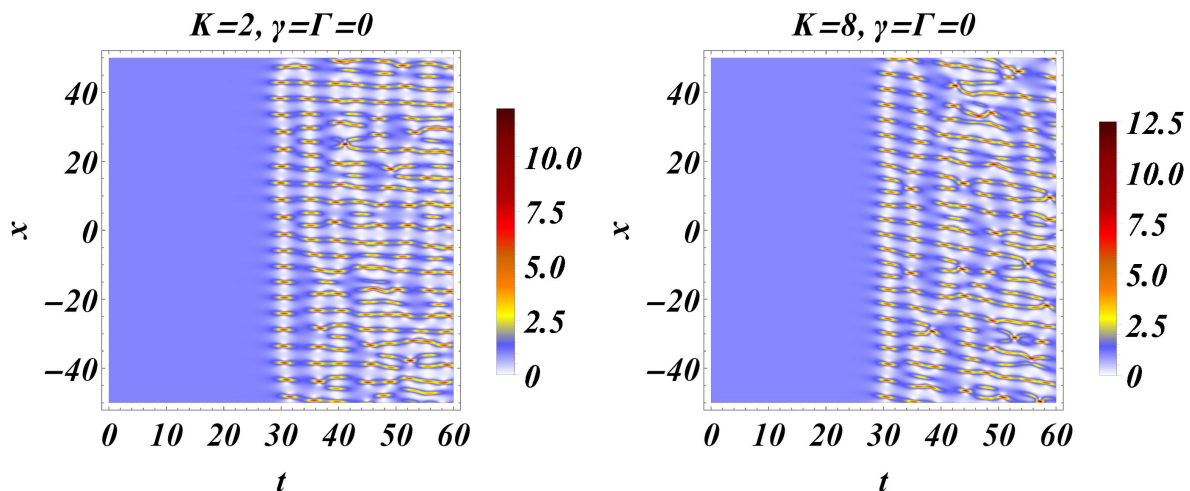


Figure 5: (Color Online) Contour plots of the spatiotemporal evolution of the density in the case of the integrable limit $\Gamma = \gamma = 0$, for two cases of initial wave-numbers. Values of the rest of the parameters: $A = 1$, $\nu = \sigma = 1$, $L = 60$.

In both cases, the dynamics are almost identical, characterized by the emergence of the vertical “first line” of extreme events, separating the spatiotemporal domain in two distinct regions: before this line, and for $t \lesssim 30$ the manifestation of MI is weak, while from the “line” and above $t \gtrsim 30$, the manifestation of MI is characterized again by the occurrence of extreme events; the line itself resembles a *spatially periodic state reminiscent of an Akhmediev breather* (see [37, Fig 3, pg. 103901-3] for similar patterns).

While in the integrable limit, we comment on the robustness of the numerical scheme and its outcomes. As complicated dynamics are discussed, it is important to make sure that numerically induced complex behavior [38, 39], due to the numerical scheme used is not present, perturbing artificially its homoclinic structure. This is done through checking the behavior of the conserved quantities in the integrable limit $\gamma = \Gamma = 0$. Indeed, in Fig. 6 the first three integrals of motion $M(t)$ [Eq. (6)], $P(t)$ [Eq. (7)] and $H(t)$ [Eq. (8)] of the unperturbed, integrable NLS equation are shown to be constant throughout the evolution. As such, our findings are numerically supported with no artificially induced phenomena entering the dynamics.

6. *Robustness of the dynamics with respect to parameters.* An important question we examine is the potential robustness of the dynamics as the various parameters are varied. Generically, it persists up to certain thresholds identified for the parameters, as suggested by the results presented in Figure 7. Concerning variations of the damping strength and amplitude of the forcing, we found that the phenomenon emerges when $\Gamma > \Gamma_{\text{thresh}}$ (for suitable fixed γ) and persists for $\gamma < \gamma_{\text{thresh}}$ (for suitable fixed Γ). Particularly, we found that the dynamics are sensitive for small increments of the damping strength $\gamma \sim \mathcal{O}(10^{-3})$, as shown in the top left panel for $\gamma = 0.02$ where the effects are weakened. Yet in this regime, the emergence of the triangular patterns persists up to a certain threshold γ_{thresh} . Similarly, the threshold $\Gamma_{\text{thresh}} \sim \mathcal{O}(10^{-3})$ was found relatively small for the given fixed set of parameters; for $\Gamma < \Gamma_{\text{thresh}}$ the dynamics were close to that of the integrable limit. For increased values of Γ , the amplitude of the first extreme events, as well as, the amplitude and the spatiotemporal density of the extreme waves within the triangular regions (and on the caustics) is increased, as shown in the top middle panel corresponding to the case of $\Gamma = 0.8$. Relevant thresholds $\sim \mathcal{O}(1)$ were identified for the rest of parameters. For $\Omega < \Omega_{\text{thresh}}$ the dynamics are like the one observed for large Γ , while for $\Omega > \Omega_{\text{thresh}}$ approaches that of

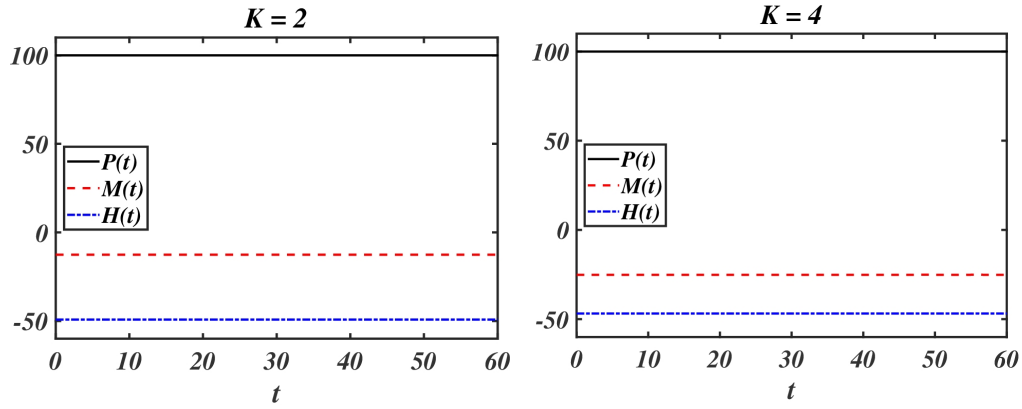


Figure 6: (Color Online) The evolution of the first three conserved quantities $P(t)$ [square of the L^2 -norm or wave action (black solid curve), $M(t)$ [momentum (dashed red curve)] and $H(t)$ [Hamiltonian (dotted blue curve)] for the integrable equation Eq. (1) with $\gamma = \Gamma = 0$, for different values of K . The rest of the parameters are as in Fig. 5. No numerical discrepancies are present as all remain constant for the duration of the evolution.

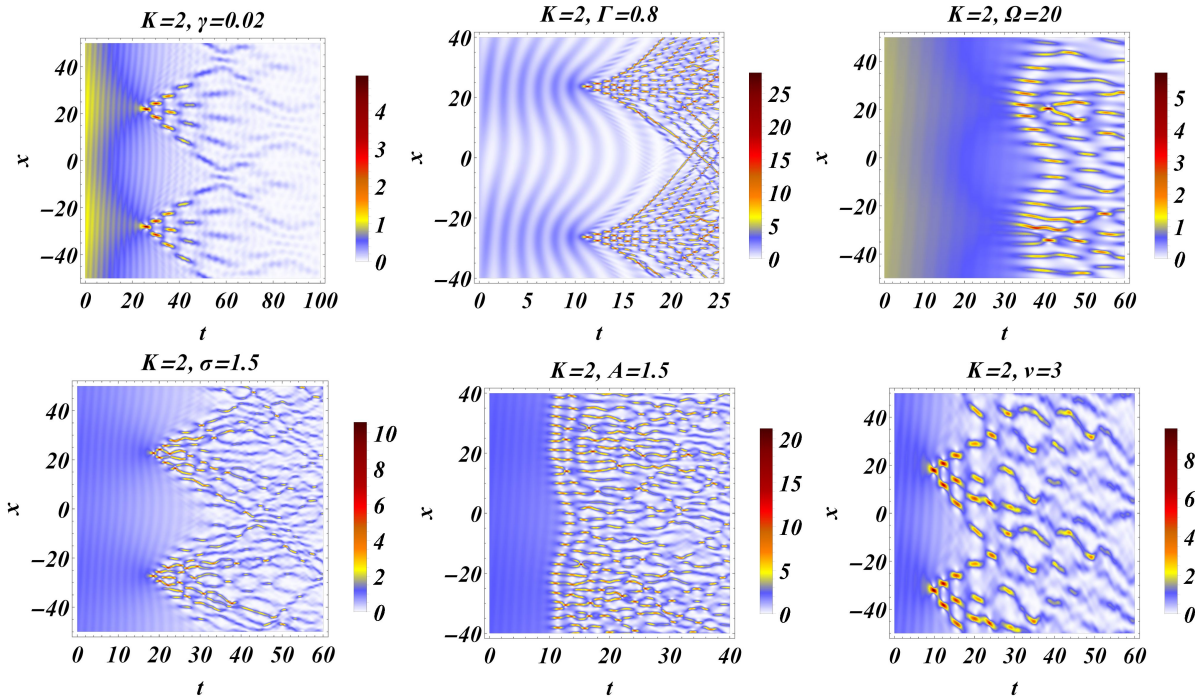


Figure 7: (Color Online) Contour plots of the spatiotemporal evolution of the density, when a parameter is varied while the rest of them are fixed as in Fig. 1.

the integrable limit, as shown in the top right panel for $\Omega = 20$; this is explained as in the limit of large Ω , the time-period of the oscillations which is dictated by the frequency of the driver should tend to zero. A behavior similar to the one of large Ω is observed for $\sigma > \sigma_{\text{thresh}}$ and larger amplitudes of the initial condition $A > A_{\text{thresh}}$ where the effects are enhanced; see the bottom left and middle panels for $\sigma = 1.5$ and $A = 1.5$, respectively. The bottom right panel for $\nu = 3$ verifies that for increased $\nu > \nu_{\text{thresh}}$, the triangular patterns are disordered due to the increased dispersion.

III. DIAGNOSTICS FOR THE EMERGENCE OF EXTREME EVENTS FROM FUNCTIONALS

A. Conserved quantities, balance laws and attractors

We start the analytical considerations by discussing the conserved quantities and energy balance laws for (1). These laws will enable us to justify the behavior of the functionals which will act as diagnostics for the time of occurrence of extreme events. We also recall that from the energy balance laws, suitable parametric estimates can be derived for the solutions, leading to the well known result of the existence of a global attractor for the corresponding infinite dimensional dynamical system [40–42]. This it will be particularly useful in analysing the long-time asymptotics for certain parametric regimes of interest.

The problem is formulated in the Sobolev spaces of $2L$ -periodic functions on the fundamental interval $\mathcal{Q} = [-L, L]$. For the sake of completeness, we recall their definition:

$$\begin{aligned} H_{\text{per}}^k(\mathcal{Q}) = \{ & u : \mathcal{Q} \rightarrow \mathbb{C}, \quad u \text{ and } \frac{\partial^j u}{\partial x^j} \in L^2(\mathcal{Q}), \quad j = 1, 2, \dots, k; \\ & u(x), \text{ and } \frac{\partial^j u}{\partial x^j}(x) \text{ for } j = 1, 2, \dots, k-1, \text{ are } 2L\text{-periodic} \}. \end{aligned} \quad (11)$$

The change of variables $u \rightarrow u \exp(-i\Omega t)$, transforms the non-autonomous (1), to its autonomous form:

$$iu_t + \frac{\nu}{2}u_{xx} + \sigma|u|^2u = \Omega u - i\gamma u + \Gamma. \quad (12)$$

We proceed to the study of the behavior of various functionals for the solutions. First, motivated by Ref. [43], we consider the following modified averaged momentum functional:

$$I(t) = \frac{\exp(2\gamma t)}{2L} \text{Im} \int_{\mathcal{Q}} u(x, t) \overline{u_x}(x, t) dx. \quad (13)$$

The modification is taking on account the exponential term $\exp(2\gamma t)$ due to the presence of the linear loss term in (1). Due to this, $I(t)$ is a now conserved quantity for (1), despite the presence of damping and forcing.

Proposition III.1 *For any initial condition $u_0 \in H_{\text{per}}^1(\mathcal{Q})$, the modified momentum functional (13) is an integral of motion for the damped and forced (1) with $\gamma, \Gamma > 0$, i.e.*

$$\frac{d}{dt} I(t) = 0. \quad (14)$$

Consequently, the momentum functional $M(t)$ defined in Eq. (6) decays exponentially:

$$M(t) = M(0) \exp(-2\gamma t), \quad \lim_{t \rightarrow \infty} M(t) = 0. \quad (15)$$

Proof: We start by differentiating (13) in time, to observe that

$$\begin{aligned} \frac{d}{dt} I(t) &= 2\gamma \frac{e^{2\gamma t}}{2L} \text{Im} \int_{\mathcal{Q}} u \overline{u_x} dx + \frac{e^{2\gamma t}}{2L} \text{Im} \int_{\mathcal{Q}} (u_t \overline{u_x} + u \overline{u_{xt}}) dx \\ &= \frac{e^{2\gamma t}}{L} \text{Im} \int_{\mathcal{Q}} \left[\gamma u \overline{u_x} + \frac{1}{2} u_t \overline{u_x} + \frac{1}{2} u \overline{u_{xt}} \right] dx \\ &= \frac{e^{2\gamma t}}{L} \text{Im} \int_{\mathcal{Q}} [\gamma u \overline{u_x} + u_t \overline{u_x}] dx + \frac{e^{2\gamma t}}{L} \text{Im} \int_{\mathcal{Q}} \left[-\frac{1}{2} u_t \overline{u_x} + \frac{1}{2} u \overline{u_{xt}} \right] dx \\ &= \frac{e^{2\gamma t}}{L} \text{Im} \int_{\mathcal{Q}} [\gamma u + u_t] \overline{u_x} dx + \frac{e^{2\gamma t}}{2L} \text{Im} \int_{\mathcal{Q}} [u \overline{u_{xt}} - u_t \overline{u_x}] dx = J_1 + J_2. \end{aligned} \quad (16)$$

We proceed to the evaluation of the integral terms J_1 and J_2 . For the first term J_1 , we substitute u_t from Eq. (12):

$$\begin{aligned} J_1 &= \frac{e^{2\gamma t}}{L} \text{Im} \int_{\mathcal{Q}} \left[\gamma u + \frac{i\nu}{2} u_{xx} + i\sigma|u|^2u + i\Omega u - \gamma u - i\Gamma \right] \overline{u_x} dx \\ &= \frac{e^{2\gamma t}}{L} \text{Im} \int_{\mathcal{Q}} \left[\frac{i\nu}{2} u_{xx} + i\sigma|u|^2u - i\Omega u - i\Gamma \right] \overline{u_x} dx. \end{aligned} \quad (17)$$

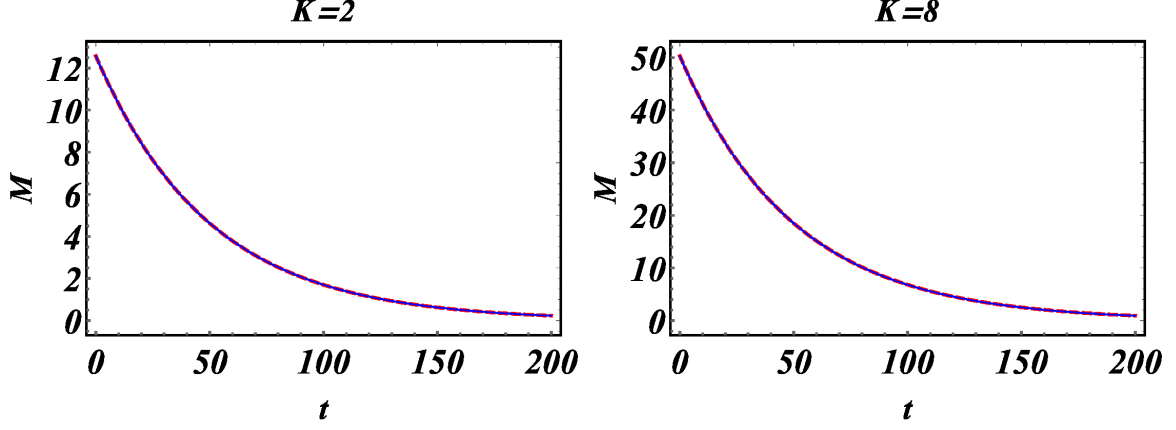


Figure 8: (Color Online) Top row: Evolution of the momentum functional $M(t)$ for two cases of the wave number K of the initial condition (2). Left panel for $K = 2$ and right panel for $K = 8$. The continuous (blue curve) traces the analytical exponential decaying law (15), and the dashed (red) curve the numerical evolution of $M(t)$.

Integration by parts and periodicity implies that the integrals of the first three terms have zero contribution. For example, setting $u = \phi + i\psi$, we have:

$$i|u|^2 u \bar{u}_x = i \{ (\phi^2 + \psi^2) [(\phi \phi_x + \psi \psi_x) + i(\phi_x \psi - \phi \psi_x)] \},$$

and therefore,

$$\begin{aligned} \text{Im} \sigma \int_{\mathcal{Q}} i|u|^2 u \bar{u}_x dx &= \sigma \int_{\mathcal{Q}} (\phi^2 + \psi^2) (\phi \phi_x + \psi \psi_x) dx = \sigma \int_{\mathcal{Q}} (|u|^2)_x |u|^2 dx \\ &= \sigma [|u|^4]_L^L - \sigma \int_{\mathcal{Q}} |u|^2 (|u|^2)_x dx. \end{aligned}$$

The last equation implies that

$$\text{Im} \sigma \int_{\mathcal{Q}} i|u|^2 u \bar{u}_x dx = 0.$$

Then, we conclude for J_1 that:

$$J_1 = -\Gamma \frac{e^{2\gamma t}}{L} \text{Im} \int_{\mathcal{Q}} i \bar{u}_x dx = 0. \quad (18)$$

For the integral J_2 of (16) we also have:

$$\begin{aligned} J_2 &= \frac{e^{2\gamma t}}{2L} \left(\text{Im} \int_{\mathcal{Q}} u \bar{u}_{xt} dx - \text{Im} \int_{\mathcal{Q}} u_t \bar{u}_x dx \right) = \frac{e^{2\gamma t}}{2L} \text{Im} [u u_t]_{-L}^L \\ &\quad - \frac{e^{2\gamma t}}{2L} \left(\text{Im} \int_{\mathcal{Q}} u_x \bar{u}_t dx + \text{Im} \int_{\mathcal{Q}} u_t \bar{u}_x dx \right) \\ &= -\frac{e^{2\gamma t}}{2L} \left(\text{Im} \int_{\mathcal{Q}} \overline{u_t \bar{u}_x} dx + \text{Im} \int_{\mathcal{Q}} u_t \bar{u}_x dx \right) = 0. \end{aligned}$$

Thus, for the damped and forced NLS (1), the modified functional $I(t)$ is an integral of motion, since from (16), it follows that $\frac{d}{dt} I(t) = 0$, i.e.,

$$\frac{\exp(2\gamma t)}{2L} \text{Im} \int_{\mathcal{Q}} u \bar{u}_x dx = \frac{1}{2L} \text{Im} \int_{\mathcal{Q}} u_0 \bar{u}_{0x} dx, \quad \bar{u}_{0x} = \bar{u}_x(x, 0). \quad (19)$$

From (19) we derive the decaying law (15). \square

The value of Proposition III.1 is multifold. First, it is interesting to justify that in the case of the damped and forced NLS (1) the forcing is not affecting the behavior of the momentum (6) which decays exponentially as in the unforced case. Second, as in the case of the integrable NLS, it is important for the justification of the numerical results on the complex dynamics discussed above: Recalling again [38, 39], numerical complex (even chaotic) behavior may be produced by numerical schemes which do not preserve the conservation laws of the system. This is not the case in our numerical results for the damped and forced case. Fig. 8 depicts the comparison of the evolution of the momentum $M(t)$ as given analytically by (15) [continuous (blue) curve], against its numerical values [dashed (red) curve] for two cases of wave numbers $K = 2$ and $K = 8$; the rest of parameters are fixed as in the study of Fig. 1. The system is integrated for $t \in [0, 200]$, and in both cases of wave numbers we observe the excellent agreement of the numerical evolution of the momentum with the analytical prediction. In the same point of view we may examine the behavior of some other conserved quantities of the integrable limit in the damped and forced NLS (1). The power $P(t)$ satisfies when $\gamma, \Gamma > 0$ the estimate

$$P(t) \leq P(0) \exp(-\gamma t) + \frac{2\Gamma^2 L}{\gamma^2} [1 - \exp(-\gamma t)], \quad \text{for all } t > 0. \quad (20)$$

From the estimate (20), one may extract uniform boundedness of the solutions of (1) in the L^2 -norm. For the other fundamental conserved quantity of the integrable limit, the Hamiltonian energy, it can be shown that in the case of the damped and forced NLS (1), it satisfies the balance law

$$\frac{1}{4} \frac{d}{dt} H(t) = \text{Re} \int_{\mathcal{Q}} i\gamma u \bar{u}_t dx + \Omega \text{Re} \int_{\mathcal{Q}} u \bar{u}_t dx - \Gamma \text{Re} \int_{\mathcal{Q}} \bar{u}_t dx. \quad (21)$$

Next, we may consider the functional

$$F(t) = \frac{\nu}{4} \int_{\mathcal{Q}} |u_x|^2 dx - \frac{\sigma}{4} \int_{\mathcal{Q}} |u|^4 dx - \frac{\Omega}{2} \int_{\mathcal{Q}} |u|^2 dx + \Gamma \text{Re} \int_{\mathcal{Q}} u dx, \quad (22)$$

for which, the following differential inequality holds:

$$\frac{d}{dt} F(t) + \gamma F(t) \leq \frac{\gamma \Omega}{2} \|u\|_{L^2}^2 + \frac{3\gamma \sigma}{8L} \|u\|_{L^2}^4 + \frac{9\gamma \sigma^2}{4\nu} \|u\|_{L^2}^6. \quad (23)$$

The differential inequality (23) if combined with the uniform in time estimates for P , it also provides uniform in time estimates in the $H_{\text{per}}^1(\mathcal{Q})$ -norm. Then, one may use the energy balance equation (21) and the energy method of [44], [45] (together with the compactness of the embedding $H_{\text{per}}^1(\mathcal{Q}) \subset L^2(\mathcal{Q})$), to prove the following result.

Theorem III.1 *Let $\nu, \sigma, \gamma > 0$ and $\Gamma, \Omega \in \mathbb{R}$. Then, for the dynamical system $\varphi_t : H_{\text{per}}^1(\mathcal{Q}) \rightarrow H_{\text{per}}^1(\mathcal{Q})$ defined from equation (1) when supplemented with the periodic boundary conditions (3), there exists a global attractor \mathcal{A} in $H_{\text{per}}^1(\mathcal{Q})$.*

The global attractor is invariant under the flow, i.e., $\varphi_t(\mathcal{A}) = \mathcal{A}$, for all $t \geq 0$, and

$$\text{dist}(\varphi_t(u_0), \mathcal{A}) \rightarrow 0, \quad \text{as } t \rightarrow \infty, \quad \text{for all } u_0 \in H_{\text{per}}^1(\mathcal{Q}). \quad (24)$$

The distance in (24) is defined as a distance between a point u and a set \mathcal{S} of $H_{\text{per}}^1(\mathcal{Q})$:

$$\text{dist}(u, \mathcal{S}) = \inf_{w \in \mathcal{S}} \|u - w\|_{H_{\text{per}}^1(\mathcal{Q})}. \quad (25)$$

For the parametric regimes we are interested in our simulations, the structure of the global attractor will be revealed in the next section.

B. Norm diagnostics for rogue wave dynamics.

It follows from Proposition III.1 that although the momentum functional $M(t)$ involves the gradient of the solution u_x , it does not capture the manifestation of the PRW-extreme events, which are characterized by the emergence of steep gradients. Hence, we examine numerically the evolution of the functionals $P(t)$ and $H(t)$, as well as, the components of the Hamiltonian $D(t)$ and $\|u(t)\|_{L^4}^4$ given in Eq. (4) and Eq. (5), respectively.

The top panels of Fig. 9 and Figure 10 depict the dynamics of the functionals $D(t)$ [continuous (black) curve] and of $\|u(t)\|_{L^4}^4$ [dashed (red) curve], for two cases of the wave number of the initial condition, $K = 2$ and $K = 4$

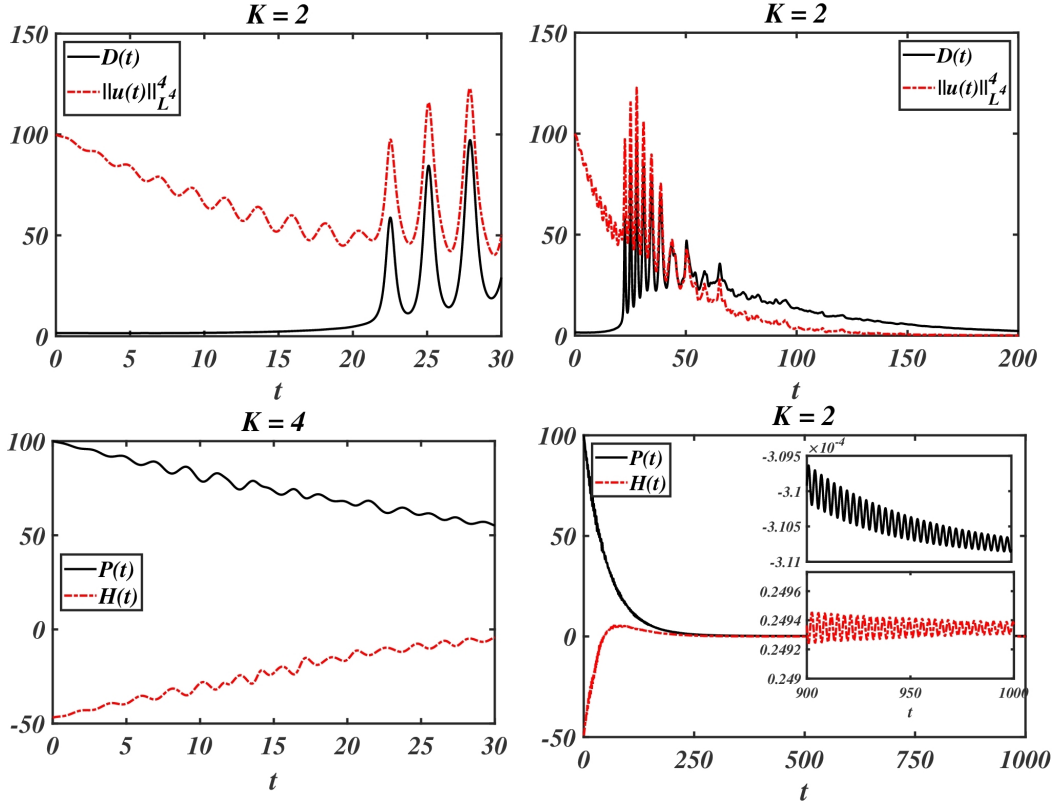


Figure 9: (Color Online) Top left panel: evolution of $D(t)$ (see (4)) [continuous (black) curve] and of $\|u(t)\|_{L^4}^4$ [dashed (red) curve], for wave number $K = 2$ of the initial condition (2), when $t \in [0, 30]$. Top right panel: Same as above but for $t \in [0, 200]$. Bottom left panel: Evolution of the power $P(t)$ [continuous (black) curve] and of the Hamiltonian $H(t)$ [dashed (red) curve], for $K = 2$, when $t \in [0, 30]$. Bottom right panel: Same as above for $t \in [0, 1000]$. The insets portray a zoom-in of the evolution when $t \in [900, 1000]$.

respectively. The rest of parameters are still fixed as in the study of Fig. 1. The bottom panels of Figure 9 and Figure 10 depict the dynamics of the power $P(t)$ [continuous (black) curve] and of the Hamiltonian $H(t)$ [dashed (red) curve].

We observe important differences but also similarities between the behavior of $D(t)$ and $\|u(t)\|_{L^4}^4$, against $P(t)$ and $H(t)$. The differences are the following:

- The functionals $D(t)$ and $\|u(t)\|_{L^4}^4$ detect the emergence of extreme events at the same time t^* of their occurrence, as it can be easily inferred by a comparison of the top panels of Figures 9-10 and Figures 1-2 (top and bottom left panels). This detection is manifested by the *local maxima possessed by $D(t)$ and $\|u(t)\|_{L^4}^4$, at the time of occurrence of the rogue waves*. Furthermore, both functionals detect the time interval where a transient enhanced instability occurs, accompanied by the emergence of extreme events, while afterwards, both functionals demonstrate stabilization manifested by a converging behavior.
- The power $P(t)$ and the Hamiltonian $H(t)$ do not exhibit extrema at the time t^* of occurrence of the extreme events. Both functionals exhibit (modulo oscillations) a uniform with respect to time converging behavior, without detecting the interval of the above enhanced transient instability.

The simulations suggest some other features:

- Prior to the detection of the emergence of the first rogue wave accompanied by the manifestation of the first local maximum, the functional $D(t)$ is almost constant for a finite time interval $[0, T_s]$ ($T_s \approx 5$ in the case $K = 2$ and $T_s \approx 10$ in the case $K = 4$). This is the time interval where the instability is not yet strongly manifested; the initial condition has the form of a plane wave and within this time interval, the solution resembles closely a plane wave. For instance, we may assume that for short time intervals prior the manifestation of the instability,

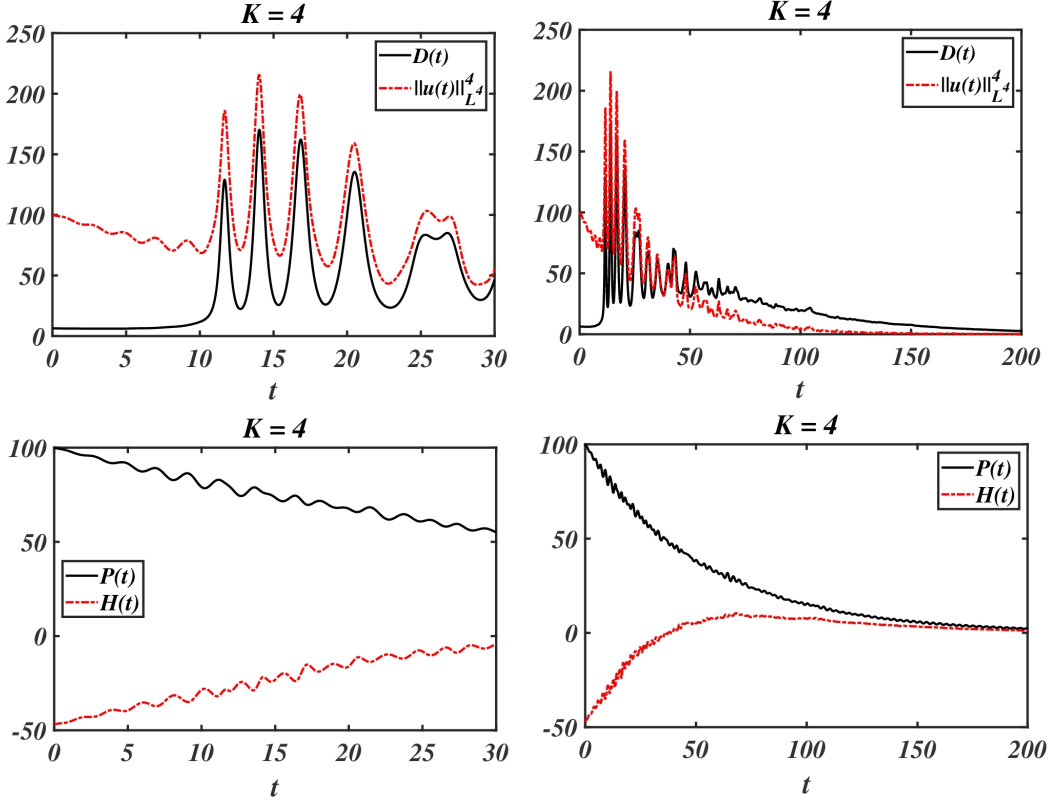


Figure 10: (Color Online) Top left panel: evolution of $D(t)$ (see (4)) [continuous (black) curve] and of $\|u(t)\|_{L^4}^4$ [dashed (red) curve], for wave number $K = 4$ of the initial condition (2), when $t \in [0, 30]$. Parameters: $\gamma = 0.01$, $\Gamma = 0.1$, $\Omega = -2$. Top right panel: Same as above but for $t \in [0, 200]$. Bottom left panel: Evolution of the power $P(t)$ [continuous (black) curve] and of the Hamiltonian $H(t)$ [dashed (red) curve], for $K = 4$, when $t \in [0, 30]$. Bottom right panel: Same as above for $t \in [0, 200]$.

like $[0, T_s]$, the solution can be approximated as

$$u(x, t) \approx Ae^{i\theta(x, t)}, \quad \theta(x, t) \approx kx - \omega t, \quad k \approx \frac{K\pi}{L}, \quad \omega \approx \Omega. \quad (26)$$

The approximation (26) implies that $D(t) \approx \frac{2A^2 K^2 \pi^2}{L}$, for $t \in [0, T_s]$. For $t \gtrsim T_s$, the instability growth becomes exponential and reaches a local maximum due to the presence of the first rogue wave. The subsequent appearance of rogue waves is detected within the time interval where $D(t)$ exhibits its large amplitude oscillations. The appearance of the local maxima of $D(t)$ is explained by the steep gradients of the emerged rogue waves.

- For $t \in [0, T_s]$ and within the time interval of the enhanced instability (where the local maxima appear of both functionals), the graph $\|u(t)\|_{L^4}^4$ is above the graph of $D(t)$. We also note the decreasing oscillatory behavior of $\|u(t)\|_{L^4}^4$ prior to the appearance of its first local maximum. Both effects can be explained by the balance law for the Hamiltonian $H(t)$ given in Eq. (21) and the approximation (26): Substitution of (26) into the right-hand side of (21) yields that

$$\frac{1}{4} \frac{d}{dt} H(t) \approx -2\gamma A \omega L + \frac{A\Gamma\omega}{K} \sin(kL) \sin(\omega t) \approx -2\gamma A \Omega L. \quad (27)$$

For the parameter values $\gamma = 0.01$, $\Gamma = 0.1$, $\Omega = -2$ considered in the numerical studies of Figures 9 and 10, the right-hand side of (27) is positive for $t \in (0, T_s]$; Thus for $t \in (0, T_s]$, the Hamiltonian $H(t)$ is increasing as found in the numerical simulations. Returning to (27), by integration with respect to time for arbitrary $t \in (0, T_s]$, we get

$$\begin{aligned} H(t) &\approx H(0) - 8\gamma A \omega L t + \frac{16A\Gamma \sin(kL)}{k^2} \cos \omega t - \frac{8A\Gamma \sin(kL)}{k^2} \\ &\approx H(0) - 8\gamma A \Omega L t, \quad t \in (0, T_s). \end{aligned} \quad (28)$$

For the given set of parameters for Figs. 9 and 10, the right-hand side of (28) captures qualitatively the superposition of linear and oscillatory growth of $H(t)$ observed in the numerics for the short time intervals $(0, T_s]$. Furthermore, from (28) and the definition of the Hamiltonian (8), we see that $\|u(t)\|_{L^4}^4$ is given by

$$\|u(t)\|_{L^4}^4 \approx D(t) - H(0) + 8\gamma\Omega Lt. \quad (29)$$

Comparing again the graphs of $D(t)$ and $\|u(t)\|_{L^4}^4$ in Figs. 9 and 10, we see that for the given set of parameters the approximative formula (29) captures the translation of $\|u(t)\|_{L^4}^4$ over $D(t)$ and its decrease prior to the time interval of enhanced instability, since $H(0) < 0$ and $\Omega < 0$. Importantly, this translation explains that the extrema of $\|u(t)\|_{L^4}^4$ occur at the same times as of $D(t)$.

► We also examined the behavior of another important quantity, the variance

$$V(t) = \int_{\mathcal{Q}} |x|^2 |u(x, t)|^2 dx, \quad (30)$$

which may exhibit a similar behavior as $P(t)$ due to the bound

$$V(t) \leq L^2 P(t), \quad (31)$$

and the estimate (20). Indeed, we observe in Figure 11 a converging behavior of $V(t)$ for the same set of parameters and wavenumbers of the initial condition (2) as in the study of Figures figure 9 and 10.

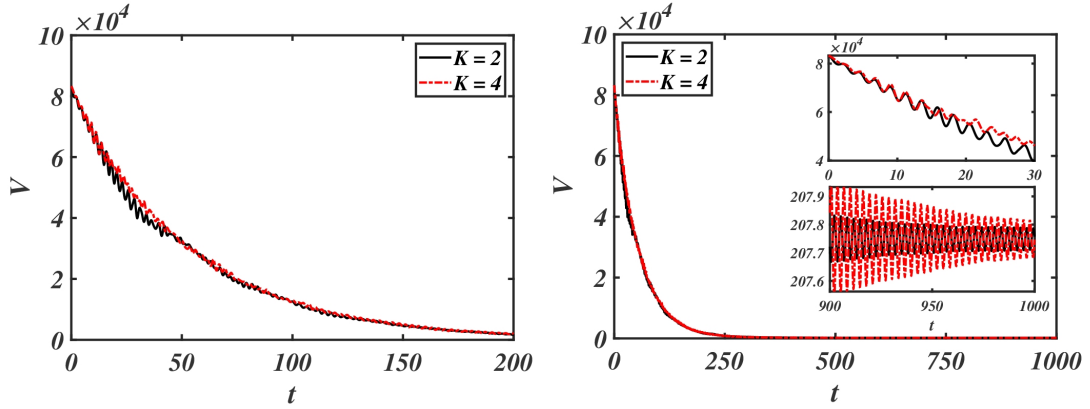


Figure 11: (Color Online) Parameters: $\gamma = 0.0$, $\Gamma = 0.1$, $\Omega = -2$. Time evolution of the variance $V(t)$ for the initial condition (2), when $K = 2$ [continuous (black) curve] and $K = 4$ [red (dashed) curve]. Left panel: time evolution for $t \in [0, 200]$. Right panel: time evolution for $t \in [0, 1000]$. The insets portray a zoom of the evolution for $t \in [0, 30]$ (upper inset) and $t \in [900, 1000]$ (bottom inset).

Summarizing all the above, we found the following: Neither of the main conserved quantities of the integrable limit $\gamma = \Gamma = 0$, may detect the emergence of rogue waves as extreme events in the transient dynamics of the initial condition (2) for the damped and forced NLS (1) $\gamma, \Gamma > 0$. Instead, *each part of the Hamiltonian energy $D(t)$ and $\|u(t)\|_{L^4}^4$ detects the emergence of rogue waves as local maxima at the times of their appearance.*

We conclude with a general comment. The diagnostic tools $D(t)$ and $\|u(t)\|_{L^4}^4$ may be used as general tools for the detection of extreme events in NLS-type equations. While we will explore further this effect elsewhere, we depict the evolution of these functionals for the integrable NLS equation in Fig. 12 with the rest of parameters fixed as in the study of Fig. 9, corresponding to the spatiotemporal dynamics depicted in the left panel Fig. 5. What is important to note here, is that the two curves are self-similar and only differ in height consistently. This is due to the conservation of energy which can be rewritten as

$$\|u(t)\|_{L^4}^4 = D(t) - H(0).$$

Thus, while the Hamiltonian is constant throughout the evolution and negates any extreme events prediction, this is not the case for its components as we also analysed for the damped and forced case.

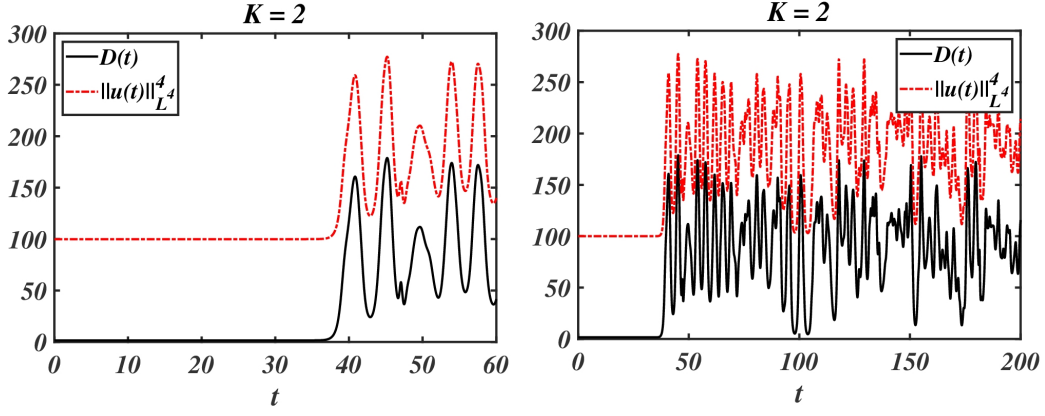


Figure 12: (Color Online) The relative study of Fig. 9 in the case of the integrable limit $\gamma = \Gamma = 0$ (see the dynamics depicted in the left panel of Fig. 5).

IV. LONG-TIME ASYMPTOTICS

In order to understand the large-time behavior of the solutions as suggested by above functionals, it is important to discuss the stability of stationary states of (1). We will carry out a stability analysis following the lines of [46]. We have set for simplicity $\mu = \nu = 1$ in (1).

Theorem IV.1 *Spatially uniform continuous wave solutions of the form*

$$u_s(t) = \phi_0 e^{i\Omega t}, \quad \phi_0 \in \mathbb{C}, \quad \Omega \in \mathbb{R}, \quad (32)$$

when they exist for (1), posses the following modulational, linear stability properties:

1. (a) *When $\Omega > 0$, they are stable with respect to small perturbations of the form $y(x, t) = z(x)e^{\lambda t}$, $z(x) = e^{-ikx}$, i.e., modulationally stable, for all $k \in \mathbb{R}$, if $|\phi_0|^2 \leq \Omega/3$.*
- (b) *When $\Omega < 0$ and $|\phi_0|^2 < \gamma$, there exists a stability band $I_{k^2} = [0, 2(-\Omega + |\phi_0|^2)] \cup [2(-\Omega + 3|\phi_0|^2), \infty)$, such that u_s is modulationally stable if $k^2 \in I_{k^2}$. Otherwise is unstable.*
2. *When $\Omega > 0$ and $|\phi_0|^2 > \Omega/3$, we distinct between the following cases:*
 - (a) *They are unstable if $|\phi_0|^2 > \max\{\gamma, \Omega/2\}$.*
 - (b) *When $\Omega/3 < |\phi_0|^2 < \Omega/2$, they are unstable if $\gamma < \Omega/2$.*

Proof: A. *Existence.* Substituting (32) into (1), we see that ϕ_0 satisfies the equation,

$$-\phi_0 \Omega + |\phi_0|^2 \phi_0 = \Gamma - i\gamma \phi_0.$$

Now, writing $\phi_0 = \alpha e^{i\theta}$, $\alpha \in \mathbb{R}$, $\theta \in (-\pi, \pi]$, the above equation leads to

$$\alpha^3 - \alpha \Omega = \Gamma e^{-i\theta} - i\gamma \alpha.$$

Separating the real and imaginary parts, gives us the system

$$\begin{aligned} \alpha^3 - \alpha \Omega &= \Gamma \cos \theta, \\ \gamma \alpha &= -\Gamma \sin \theta. \end{aligned}$$

By eliminating θ , we get

$$\alpha^6 - 2\alpha^4 \Omega + (\gamma^2 + \Omega^2) \alpha^2 = \Gamma^2,$$

and setting $\rho = \alpha^2$, we end up with a cubic algebraic equation

$$F(\rho; \gamma, \Gamma, \Omega) \equiv \rho^3 - 2\Omega \rho^2 + (\gamma^2 + \Omega^2) \rho - \Gamma^2 = 0. \quad (33)$$

Substituting $\rho = -q, q > 0$, will give us the sum of four negative terms. Hence, equation (33) can have either three positive real solutions or two complex-conjugate solutions and one real, positive. Any positive root of equation (33) defines a solution

$$\phi_0 = \sqrt{\rho}e^{i\theta}, \quad \tan \theta = \frac{\gamma}{\Omega - \rho}. \quad (34)$$

Through the substitution $\rho = y + 2\Omega/3$ (see [47, Sec. 2.3.2]), equation (33) can be transformed to the “reduced” form

$$y^3 + py + q = 0, \quad (35)$$

where $p = \gamma^2 - \Omega^2/3$ and $q = 2/3\Omega(\gamma^2 + \Omega^2/9) - \Gamma^2$.

Analysis of a such cubic equation suggests the distinction between two cases, $p \geq 0$ and $p < 0$.

- If $p \geq 0$, then $\gamma^2 \geq \Omega^2/3$ and the derivative of the equation (35) will be positive. Hence, (35) is monotone increasing and therefore, has one real solution.
- If $p < 0$, then $\gamma^2 < \Omega^2/3$ and the number of the real roots can be determined by the sign of the following quantity

$$Q = \left(\frac{\gamma^2 - \Omega^2/3}{3} \right)^3 + \left(\frac{\Omega}{3} \left(\gamma^2 + \frac{\Omega^2}{9} \right) - \frac{\Gamma^2}{2} \right)^2. \quad (36)$$

If $Q < 0$, there are three real roots and if $Q > 0$, there is one. Further analysis shows that there exist three roots if $\Gamma_-(\gamma) \leq \Gamma \leq \Gamma_+(\gamma)$, where

$$\Gamma_{\pm}(\gamma, \Omega) = \left\{ \frac{2\Omega}{3} \left(\gamma^2 + \frac{\Omega^2}{9} \right) \pm \frac{2}{3} \sqrt{\frac{1}{3} \left(\frac{\Omega^2}{3} - \gamma^2 \right)^3} \right\}^{1/2},$$

and one root otherwise.

Summarizing all the above, we conclude for the existence of stationary solutions, with the following cases:

- For $\gamma^2 \geq \frac{\Omega^2}{3}$, one real root.
- For $\gamma^2 < \frac{\Omega^2}{3}$, $\begin{cases} \text{three real roots if } \Gamma_-(\gamma) \leq \Gamma \leq \Gamma_+(\gamma), \\ \text{one real root, otherwise.} \end{cases}$

In the case where 3 positive roots exist, there are three branches of solutions defined by the critical points of F (33), namely,

$$\rho_{\pm}(\gamma, \Omega) = \frac{2\Omega}{3} \pm \frac{1}{3} \sqrt{\Omega^2 - 3\gamma^2}. \quad (37)$$

The branches are: $0 < |\phi_0|^2 \leq \rho_-(\gamma)$, $\rho_-(\gamma) < |\phi_0|^2 < \rho_+(\gamma)$ and $|\phi_0|^2 \geq \rho_+(\gamma)$.

B. Stability. Next, we examine the stability of these solutions. Substituting, $\tilde{u}(x, t) = e^{i\Omega t}u(x, t)$ into equation (1) we obtain

$$iu_t - u\Omega + \frac{1}{2}u_{xx} + |u|^2u = \Gamma - i\gamma u. \quad (38)$$

Let $\xi(x, t)$ be a small perturbation. We consider

$$u(x, t) = u_s(x) + \xi(x, t), \quad (39)$$

where $u_s(x)$ is a stationary solution of equation (38). Substituting (39) into (38), linearizing and separating the real and imaginary parts, yields the following system

$$J(y_t + \gamma y) = Hy, \quad (40)$$

where

$$J = \begin{pmatrix} 0 & -1 \\ 1 & 0 \end{pmatrix}, y(x, t) = \begin{pmatrix} \text{Re } \xi \\ \text{Im } \xi \end{pmatrix}, H = \begin{pmatrix} -\frac{1}{2}\partial_x^2 + \Omega - 3u_R^2 - u_I^2 & -2u_Ru_I \\ -2u_Ru_I & -\frac{1}{2}\partial_x^2 + \Omega - u_R^2 - 3u_I^2 \end{pmatrix}.$$

Note that, $u_s(x) = u_R + iu_I$. Substituting $y(x, t) = z(x)e^{\lambda t}$ into (40), yields the eigenvalue problem

$$Hz(x) = \mu Jz(x),$$

where $\mu = \lambda + \gamma$. The solution $u_s(x)$ will be stable if the above system does not have eigenvalues μ with real part greater than γ . In the case of the homogeneous solution $u_s(x) = \phi_0$, the eigenvalue μ and the eigenvector $z(x)$ can be found explicitly. Now, by writing $z(x) = z_0 e^{-ikx}$ and $\phi_0 = u_R + iu_I$, we get

$$(H_k - \mu J)z_0 = 0,$$

where

$$H_k = \begin{pmatrix} \frac{k^2}{2} + \Omega - 3u_R^2 - u_I^2 & -2u_R u_I \\ -2u_R u_I & \frac{k^2}{2} + \Omega - u_R^2 - 3u_I^2 \end{pmatrix}.$$

For non-trivial solutions, we require the determinant of $(H_k - \mu J)$ to be zero, implying the equation

$$-\mu^2 = \left(\frac{k^2}{2} + \Omega - |\phi_0|^2 \right) \left(\frac{k^2}{2} + \Omega - 3|\phi_0|^2 \right) \equiv G(k^2). \quad (41)$$

- When $\Omega > 0$, for $|\phi_0|^2 \leq \Omega/3$, $G(k^2) \geq 0$. Hence, $\text{Re}\mu = 0$ and the solution is modulationally stable.
- When $\Omega < 0$, we consider

$$G'(k^2) = \frac{k^2}{2} + \Omega - 2|\phi_0|^2, \quad (42)$$

where the prime denotes differentiation with respect to the variable k^2 . The critical point is

$$k_{crit}^2 = 2(2|\phi_0|^2 - \Omega) > 0, \quad (43)$$

since $\Omega < 0$, and is a global minimum since

$$G''(k^2) = \frac{1}{2} > 0. \quad (44)$$

Next, we find that $G_{min} = G(k_{crit}^2) = -|\phi_0|^4$. Hence, $\text{Re}\mu = |\phi_0|^2$ and the solution will be unstable for $|\phi_0|^2 > \gamma$.

In the case where $|\phi_0|^2 < \gamma$, we have that $G(k^2) \geq 0$ for $k^2 \in I_{k^2}$ and the solution is modulationally stable.

- When $\Omega > 0$ and $|\phi_0|^2 > \Omega/3$, we distinguish between the following cases:
 1. If $|\phi_0|^2 > \Omega/2$, we work again with (42)-(43)-(44) as in the case $\Omega < 0$, to show that for $|\phi_0|^2 > \gamma$ the solution is unstable.
 2. For $\Omega/3 < |\phi_0|^2 < \Omega/2$, the minimum occurs at $k^2 = 0$ and is equal to $G_{min} = (|\phi_0|^2 - \Omega)(3|\phi_0|^2 - \Omega)$. Therefore, the solution is unstable for

$$-(|\phi_0|^2 - \Omega)(3|\phi_0|^2 - \Omega) > \gamma^2.$$

Further analysis will show that the inequality above is valid when

$$|\phi_0|_-^2 < |\phi_0|^2 < |\phi_0|_+^2,$$

where

$$|\phi_0|_{\pm}^2 = \frac{2\Omega}{3} \pm \frac{1}{3}\sqrt{\Omega^2 - 3\gamma^2}.$$

Note that the amplitudes $|\phi_0|_{\pm}^2$ are equivalent to the critical points of F , (37). Moreover, since $|\phi_0|^2 < \Omega/2$ then $|\phi_0|_-^2 < \Omega/2$ and after some calculations, we may conclude that this instability may occur in the region $\gamma < \Omega/2$. \square

a. *Rationalization of the asymptotic behavior for $\gamma = 0.01, \Gamma = 0.1, \Omega = -2$.* Theorem IV.1 is particularly useful in explaining the long-time asymptotics observed in Fig. 9. For this purpose, we recall the notion of orbital stability and orbital asymptotic stability. The positive orbit of the flow φ_t starting at u_0 at t_0 is the set $\mathcal{O}^+(u_0) = \cup_{t \geq t_0} \varphi_t(u_0)$.

Definition IV.1 *The solution $u_*(t) \in H_{\text{per}}^1(\mathcal{Q})$ is said to be orbitally stable, if given $\epsilon > 0$, there exists some $\delta = \delta(\epsilon) > 0$, such that for any other solution $u(t)$ satisfying $\|u^*(t_0) - u(t_0)\|_{H_{\text{per}}^1(\mathcal{Q})} < \delta$, then $\text{dist}(u(t), \mathcal{O}^+(u^*(t_0))) < \epsilon$ for $t > t_0$. It is said to be asymptotically orbitally stable if it is orbitally stable and in addition, there exists a constant $\tilde{\delta} > 0$ such that if $\|u^*(t_0) - u(t_0)\|_{H_{\text{per}}^1(\mathcal{Q})} < \tilde{\delta}$, then $\lim_{t \rightarrow \infty} \text{dist}(u(t), \mathcal{O}^+(u^*(t_0))) = 0$.*

Combining Theorems III.1 and IV.1 with Definition IV.1, we have

Theorem IV.2 *Let $\nu = \sigma = 1$ and assume that the parameters $\gamma > 0, \Gamma, \Omega \in \mathbb{R}$ are chosen so that there exists a unique modulationally stable cw solution u^s of the form (32). Then it should be globally, orbitally asymptotically stable.*

Proof: Let $\hat{u}(t)$ denote the solution starting at $t_0 = 0$ from the initial condition $\hat{u}_0 = u^s(0) + \xi(x, 0)$. When the unique cw solution u_s is modulationally stable, we have $\lambda < 0$, and as its small perturbations decay, the solution $\hat{u}(t) = \varphi_t(\hat{u}_0)$ comes arbitrarily close to u_s in the sense

$$\text{dist}(\hat{u}(t), \mathcal{O}^+(u^s(0))) = \text{dist}(\varphi_t(\hat{u}_0), \mathcal{O}^+(u^s(0))) < \epsilon. \quad (45)$$

However, according to Theorem III.1, there exists a unique global attractor \mathcal{A} attracting all initial conditions u_0 , independently of the size of their $H_{\text{per}}^1(\mathcal{Q})$ - norm and thus the limiting relation (24) holds. Hence, for all initial conditions $u_0 \in H_{\text{per}}^1(\mathcal{Q})$, there exists $T_0(u_0) > 0$ such that the solutions $u(t) = \varphi_t(u_0)$, with $u(0) = u_0$ satisfy

$$\text{dist}(\varphi_t(u_0), \mathcal{A}) < \epsilon, \quad \text{for all } t > T_0. \quad (46)$$

Since (46) holds also for the initial condition \hat{u}_0 and equation (1) is actually autonomous due to (12), the uniqueness of the attractor and (45) imply that $\mathcal{A} = \mathcal{O}^+(u^s(0))$. Yet, (24) shows that

$$\lim_{t \rightarrow \infty} \text{dist}(\varphi_t(u_0), \mathcal{O}^+(u^s(0))) = 0,$$

and that u^s is globally orbitally asymptotically stable. This asymptotic orbital stability should hold even in the case where a specific stability band I_{k^2} exists as in Theorem (IV.1) 1(b), where $G(k^2) \geq 0$ ($\text{Re}\mu = 0$) when $k^2 \in I_{k^2}$ and $G(k^2) < 0$ when $k^2 \in \mathbb{R}^+ \setminus I_{k^2}$ ($\text{Re}\mu \neq 0$): even in the latter case, where $\text{Re}\mu \neq 0$, yet $\mathcal{A} = \mathcal{O}^+(u^s(0))$ should attract all initial conditions and the divergence from u_s should be only transient; after finite time of divergence from u_s , the initial condition should approach $\mathcal{A} = \mathcal{O}^+(u^s(0))$. \square

For the parameters $\gamma = 0.01, \Gamma = 0.1$ and $\Omega = -2$ used in the simulations, the algebraic equation (33) has only one real root

$$\rho_s \approx 0.0025 = |\phi_0^s|^2. \quad (47)$$

This is in accordance with the analysis of Theorem IV.1, since for the above choice of parameters the quantity Q defined in (36) is found to equal $Q \approx 0.003 > 0$. Thus, there exists a unique stationary solution defined by (32), (34) and (47),

$$u_s(t) = \phi_0^s e^{i\Omega t}, \quad \phi_0^s = \sqrt{\rho_s} e^{i\theta_s}, \quad \tan \theta_s = \frac{\gamma}{\Omega - \rho_s}.$$

with $\sqrt{\rho_s} \approx 0.05$, $\tan \theta_s \approx -0.005$. Now, this small amplitude cw u_s satisfies the stability criterion of Theorem IV.1 1(b), since $\Omega < 0$ and $|\phi_0^s|^2 < \gamma$. Then, applying Theorem IV.2, we extract its global asymptotic stability. Thus, all initial conditions should converge to the small amplitude cw u_s , and this also holds for the initial condition (2) with $A = 1$ and $K = 2$, as shown by the convergence of the energy and norm quantities discussed in Figures 9 and 10.

We present a numerical illustration of the results stated in Theorem IV.1 and Theorem IV.2. Figure 13 shows the spatiotemporal behavior of the solutions when $\nu = \sigma = 1, \gamma = 0.1, \Gamma = 1, \Omega = 1$. The initial condition is (2) with $A = 1, K = 2$ and $L = 50$. For this set of parameters there exist again one spatially uniform cw solution defined by the real root of the equation (33)

$$\rho_u = 1.69 = |\phi_0^u|^2.$$

Since $|\phi_0^u|^2 > \max\{\gamma, \Omega/2\} = 0.5$, the solution is unstable according to the instability criterion of Theorem IV.1 2(b). In the contour plot shown in the left panel for $t \in [0, 16]$, we still observe the emergence of extreme events on

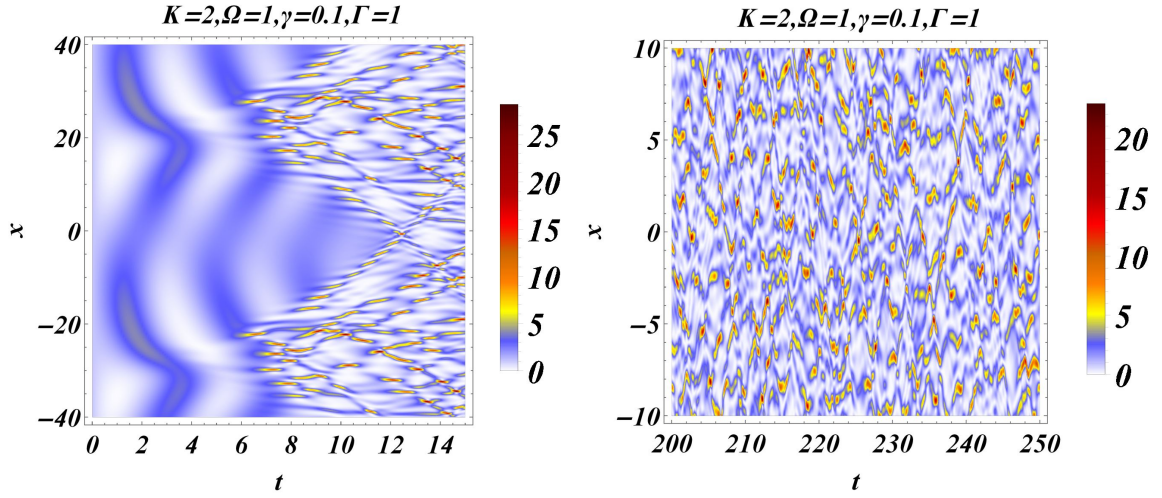


Figure 13: (Color Online) Parameters (1)-(3): $\nu = \sigma = 1$, $\gamma = 0.1$, $\Gamma = 1$, $\Omega = 1$. Dynamics of the cw-initial condition (2) for $A = 1$, $K = 2$, and $L = 50$. The left panel shows the spatiotemporal evolution of the density for $x \in [-40, 40]$ and $t \in [0, 15]$. The right panel offers a magnification of the patterns observed in the left panel, for $x \in [-10, 10]$ and $t \in [200, 250]$.

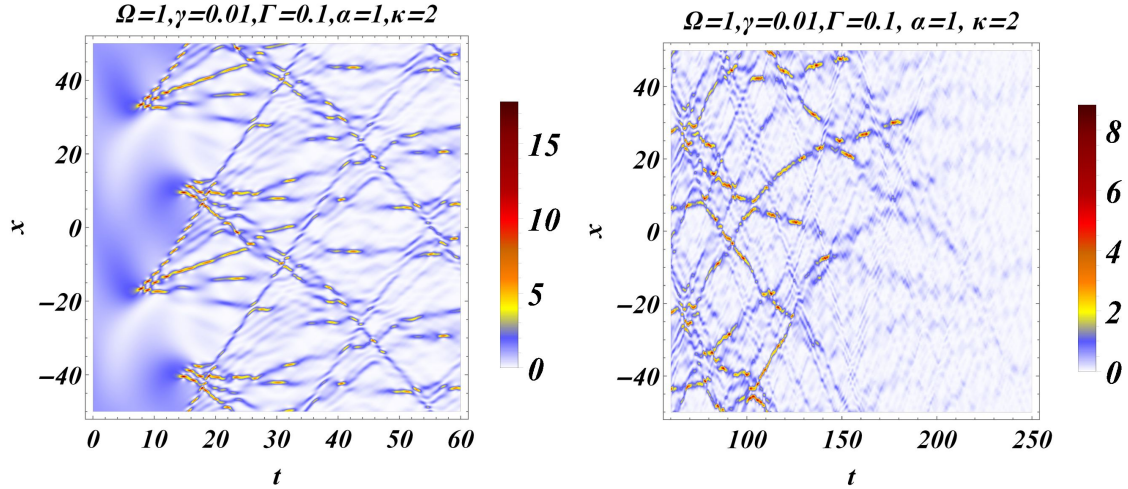


Figure 14: (Color Online) Parameters (1)-(3): $\nu = \sigma = 1$, $\gamma = 0.01$, $\Gamma = 0.1$, $\Omega = 1$. Dynamics of the initial condition (49) for $a = 1$, $\kappa = 2$, and $L = 50$. The left panel shows the spatiotemporal evolution of the density for $x \in [-L, L]$ and $t \in [0, 15]$. The right panel depicts the spatiotemporal evolution, for $x \in [-L, L]$ and $t \in [60, 250]$.

the top of two distinct “tree”-patterns. However, they do not possess the structure observed in Figure 1 and 3. The system exhibits complex spatiotemporal behavior as clearly shown in the right panel, for $t \in [200, 250]$.

A second numerical example considers the case of parameters $\nu = \sigma = 1$, $\gamma = 0.01$, $\Gamma = 0.1$, $\Omega = 1$. For these parameters, the quantity Q defined in (36) is found $Q \approx -0.0003 < 0$ and the equation (33) has three real roots

$$\rho_1^s = 0.01 = |\phi_0^{s,1}|^2, \quad \rho_2^u = 0.98 = |\phi_0^{u,2}|^2, \quad \rho_3^u = 1 = |\phi_0^{u,3}|^2. \quad (48)$$

The above roots define three cw solutions of the form (32), namely, $u_s^{s,1}$, $u_s^{u,2}$ and $u_s^{u,3}$ respectively. The solution $u_s^{s,1}$ is asymptotically stable due to Corollary IV.2 as it satisfies $|\phi_0^{s,1}|^2 < \Omega/3 = 1/3$, i.e., the stability criterion of Theorem IV.1 1(a). The other two solutions $u_s^{u,2}$ and $u_s^{u,3}$ are unstable since they satisfy the instability criterion $|\phi_0^{u,2}|^2, |\phi_0^{u,3}|^2 > \Omega/2 = 0.5$ of Theorem IV.1 2(a). Figure 14 depicts the spatiotemporal evolution of the initial condition

$$u_0(x) = u_s^{1,s}(0) + a \exp\left(\frac{i\kappa\pi x}{L}\right), \quad (49)$$

for $a = 1$, $\kappa = 2$, $L = 50$. The initial condition (49) with $a = 1$ is a large amplitude perturbation of the cw solution $u_s(t)$. The instability illustrated in the left panel, manifested again by the emergence of extreme events, is transient, as predicted by Corollary IV.2. In the right panel it is shown that solution approaches the asymptotically stable cw $u_s^{s,1}$. The convergence becomes even more evident as verified in Fig. 15, where the evolution of the density of the solution $|u(x^*, t)|^2$ at a specific point $x = x^*$ is plotted. This x^* is chosen to be the point where the solution exhibits an extreme spot, here $x^* = 10$, as seen in the left panel of Fig. 14. The plot depicts the convergence of the density to the amplitude of the asymptotically orbitally stable cw, as predicted.

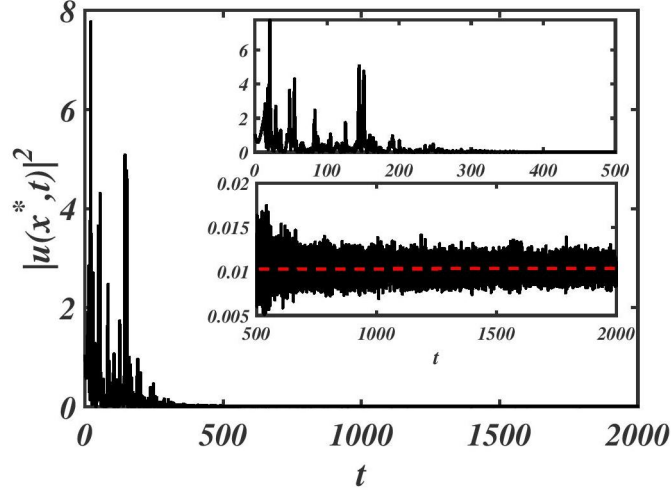


Figure 15: (Color Online) Dynamics of the density $|u(x^*, t)|^2$ [continuous (black) curve], for fixed $x^* = 10$ and the initial condition and parameters of Fig. 14. Asymptotic orbital stability of the cw $u_s^{s,1}$ with amplitude $\rho_1^s = 0.01 = |\phi_0^{s,1}|^2$ marked by the red (dashed) line (see the discussion for the amplitudes given in (48)).

b. The case $K = 1$ of the wave number of the initial condition (2). We conclude with a comment for the case $K = 1$ of the wave number of the plane wave initial condition which may also explain the formation of the dendritic patterns for higher wavenumbers. To assist us on this, we plot in Fig. 16 the spatiotemporal evolution of the density $|u(x, t)|^2$ of the initial condition (2) for $K = 1$, while all other parameters are $\Omega = -2$, $\gamma = 0.01$, $\Gamma = 0.1$, as in the case of the study of Fig. 1 and $L = 200$.

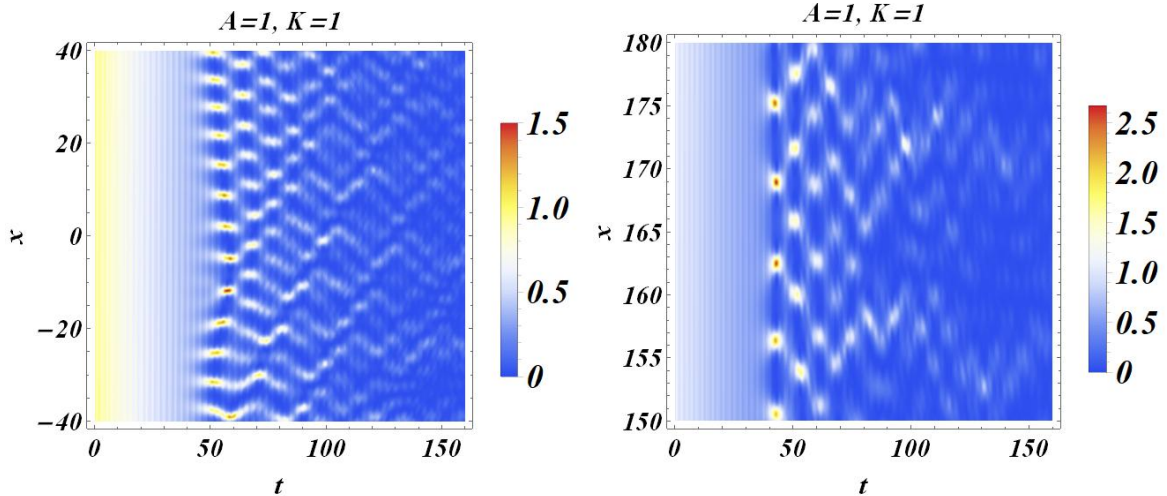


Figure 16: (Color Online) Parameters (1)-(3): $\nu = \sigma = 1$, $\gamma = 0.01$, $\Gamma = 0.1$, $\Omega = -2$. Dynamics of the initial condition (2) for $A = 1$, $K = 1$, and $L = 200$. The left panel shows the spatiotemporal evolution of the density for $x \in [-40, 40]$ and $t \in [0, 160]$. The right panel depicts the spatiotemporal evolution, for $x \in [150, 180]$ and $t \in [0, 160]$.

The two panels present two different regions. As one can readily see, the patterns observed in Fig. 1 are missing and the dynamics are found to be essentially different compared to the case $K \geq 2$. However, these figures may be

used to provide a useful understanding of the potential mechanism that may lead to the formation of the dendritic patterns observed in the case $K \geq 2$.

Indeed, noting that in the early stages of the evolution linear effects are more dominant, a plane wave initial condition will behave as a solution to the linear problem, and as such, will be subject to linear superposition. The single maximum/minimum initial state evolves as above. If more maxima/minima are added, the initial states around the minima/maxima will also undergo such evolution, but now, constructive and destructive interference may allow for more intricate patterns to form. The constructive interference will lead to the peaks of the dendritic structure, while destructive interference will leave some small amplitude waves on the constant background (seen in all numerical simulations), which have no effect on the overall phenomenon.

We also note that the dynamics we observed when $K = 1$ is no exception to the findings of the article suggested by Theorems IV.1 and IV.2, which seem to be rather sharp: Since the amplitude of the initial condition satisfies $A^2 = 1 > \gamma$, we expect, according to the instability case 1(b) of Theorem IV.1, transient modulational instabilities and then convergence to the orbitally stable cw state of amplitude (47), as in the case of $K = 2$. On the other hand, when switching the initial amplitude in order to satisfy the stability criterion 1(b) of Theorem IV.1 $A^2 < \gamma$ with $k^2 \in I_{k^2}$, we don't expect transient instabilities prior the convergence to the asymptotically stable cw state. This is indeed the case when $A = 0.09$ ($A^2 = 0.0081 < \gamma = 0.01$) and $K = 1$ which corresponds to $k^2 = 0.0002 \in I_{k^2}$, as shown in the evolution of the initial condition in Fig. 17.

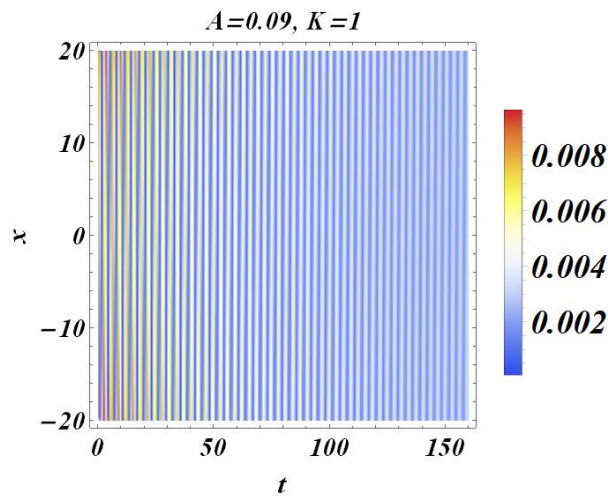


Figure 17: (Color Online) Parameters (1)-(3): $\nu = \sigma = 1$, $\gamma = 0.01$, $\Gamma = 0.1$, $\Omega = -2$. Dynamics of the initial condition (2) for $A = 0.09$, $K = 1$, and $L = 200$. The panel shows the spatiotemporal evolution of the density for $x \in [-20, 20]$ and $t \in [0, 160]$.

V. CONCLUSIONS

In this paper, we examined the dynamics of the linearly damped and time-periodically driven Schrödinger equation, initiated by the simplest initial condition, namely, a single mode plane wave. This gives rise to highly non-trivial transient dynamics manifested by the birth of rogue waves reminiscent of the Peregrine soliton in terms of its temporal decay and spatial profile. We also identified the formation of spatiotemporal patterns resembling the one observed in the semiclassical Hamiltonian limit. Our explorations justified that this behavior is far from the one of the integrable limit and discussed its robustness as the parameters of the model are varied. We also found suitable functional type diagnostics for the time of occurrence of the rogue waves and commented on their spatial predictability as dictated by the initial wave number; the array formed by the first extreme events possess the same spatial wavelength as the initial condition. The asymptotic behavior of solutions for the parametric regimes examined in the simulations was justified by the orbital stability of stationary states of the model.

We believe that our findings may be used as predicts and/or controlling tools for the detection/generation of extreme events in systems where the NLS equation is the underlying model. Further studies may include more general initial conditions in the form of a superposition of such plane waves and more general norm-based diagnostic tools. Relevant

investigations are in progress, and results will be reported in upcoming works.

-
- [1] A. D. Cattrell, M. Srokosz, B. I. Moat and R. Marsh, *Can rogue waves be predicted using characteristic wave parameters?*, J. Geophys. Res. Oceans **123** (2018), 5624–5636.
 - [2] A. V. Slunyaev, *Predicting Rogue Waves*, Moscow Univ. Phys. **72** (2017), 236–249.
 - [3] M. Farazmand and T. P. Sapsis, *Reduced-order prediction of rogue waves in two-dimensional deep-water waves*, J. Comput. Phys. **340** (2017), 418–434.
 - [4] A. L. Islas, and C. M. Schober, *Predicting rogue waves in random oceanic sea states*, Phys. Fluids **17** (2005), 031701.
 - [5] E. Zakharov and L. A. Ostrovsky, *Modulation instability: the beginning*, Phys. D **238** (2009), 540–548.
 - [6] A. Slunyaev, A. Sergeeva and E. Pelinovsky, *Wave amplification in the framework of forced nonlinear Schrödinger equation: The rogue wave context*, Phys. D **303** (2015), 18–27.
 - [7] C. Kharif and J. Touboul, *Under which conditions the Benjamin-Feir instability may spawn an extreme wave event: A fully nonlinear approach*, Eur. Phys. J. Special Topics **185** (2010), 159–168.
 - [8] C. Kharif, R. A. Kraenkel, M. A. Manna and R. Thomas, *The modulational instability in deep water under the action of wind and dissipation*, J. Fluid Mech. **664** (2010), 138–149.
 - [9] A. Chabchoub, N. P. Hoffmann, and N. Akhmediev, *Rogue Wave Observation in a Water Wave Tank*, Phys. Rev. Lett. **106** (2011), 204502.
 - [10] D. R. Solli, C. Ropers, P. Koonath, and B. Jalali, *Optical rogue waves*, Nature **450** (2007), 1054.
 - [11] H. Bailung, S. K. Sharma, and Y. Nakamura, *Observation of Peregrine Solitons in a Multicomponent Plasma with Negative Ions*, Phys. Rev. Lett. **107** (2011), 255005.
 - [12] D. H. Peregrine, *Water waves, nonlinear Schrödinger equations and their solutions*, J. Austral. Math. Soc. B **25** (1983), 16–43.
 - [13] N. N. Akhmediev, V. M. Eleonskii, and N. E. Kulagin, *Exact first order solutions of the nonlinear Schrödinger equation*, Theor. Math. Phys. **72** (1987), 809–818.
 - [14] M. Onorato and D. Proment, *Approximate rogue wave solutions of the forced and damped nonlinear Schrödinger equation for water waves*, Phys. Lett. A **376** (2012), 3057–3059.
 - [15] M. Brunetti, N. Marchiando, N. Berti, J. Kasparian, *Nonlinear fast growth of water waves under wind forcing* Phys. Lett. A **378** (2014), 1025–1030.
 - [16] A. Ankiewicz, N. Devine, N. Akhmediev, *Are rogue waves robust against perturbations?*, Phys. Lett. A **373** (2009), 3997–4000.
 - [17] A. Calini and C. M. Schober, *Dynamical criteria for rogue waves in nonlinear Schrödinger models*, Nonlinearity **25** (2012), R99–R116.
 - [18] Y. Wang, L. Song, L. LI and B. A. Malomed, *High-power pulse trains excited by modulated continuous waves*, J. Opt. Soc. Am. B **32** (2015), 2257–2263.
 - [19] L. H. Wang, K. Porsezian, and J. S. He, *Breather and rogue wave solutions of a generalized nonlinear Schrödinger equation*, Phys. Rev. E **87**, 053202 (2013), 1–10.
 - [20] A. Ankiewicz, Y. Wang, S. Wabnitz, and N. Akhmediev, *Extended nonlinear Schrödinger equation with higher-order odd and even terms and its rogue wave solutions*, Phys. Rev. E **89** (2014), 012907.
 - [21] Y. Yang, Z. Yan and B. A. Malomed, *Rogue waves, rational solitons, and modulational instability in an integrable fifth-order nonlinear Schrödinger equation*, Chaos **25** (2015), 103112.
 - [22] Y. Kivshar and B. Malomed, *Dynamics of solitons in nearly integrable systems*, Rev. Mod. Phys. **61** (1989), 763–915.
 - [23] K. Nozaki, N. Bekki, *Chaos in a perturbed nonlinear Schrödinger equation*, Phys. Rev. Lett. **50** (1983), 1226–1229.
 - [24] K. Nozaki, N. Bekki, *Solitons as attractors of a forced dissipative nonlinear Schrödinger equation*, Phys. Lett. A **102** (1984), 383–386.
 - [25] K. Nozaki and N. Bekki, *Low dimensional chaos in a driven damped nonlinear Schrödinger equation*, Phys. D **21** (1986), 381–393.
 - [26] Y. Li and D. W. McLaughlin, *Morse and Melnikov functions for NLS PDE's*, Comm. Math. Phys. **162** (1994), 175–214.
 - [27] G. Haller and S. Wiggins, *Multi-pulse jumping orbits and homoclinic trees in a modal truncation of the damped-forced nonlinear Schrödinger equation*, Phys. D **85** (1995), 311–347.
 - [28] D. Cai, D. W. McLaughlin, and J. Shatah, *Spatiotemporal chaos and effective stochastic dynamics for a near-integrable nonlinear system*, Phys. Lett. A **253** (1999), 280–286.
 - [29] E. G. Charalampidis, J. Cuevas-Maraver, D. J. Frantzeskakis, P. G. Kevrekidis, *Rogue waves in ultracold bosonic seas*, Rom. Rep. Phys. **70** (2018), 1–26.
 - [30] M. Bertola and A. Tovbis, *Universality for the focusing nonlinear Schrödinger equation at the gradient catastrophe point: Rational breathers and poles of the Trictrouqué solution to Painlevé*, Comm. Pure Appl. Math. **66** (2009), 678–752.
 - [31] R. H. J. Grimshaw and A. Tovbis, *Rogue Waves: analytical predictions*, Proc. R. Soc. A **469** (2013), 20130094.
 - [32] A. Tikan, C. Billet G. El, A. Tovbis, M. Bertola, T. Sylvestre, F. Gustave, S. Randoux, G. Genty, P. Suret, and J. M. Dudley, *Universality of the Peregrine soliton in the focusing dynamics of the cubic nonlinear Schrödinger equation*, Phys. Rev. Lett. **119** (2017), 033901.
 - [33] G. Fotopoulos, D. J. Frantzeskakis, N. I. Karachalios, P. G. Kevrekidis, V. Koukoulouyannis and K. Vetas, *Extreme wave*

- events for a nonlinear Schrödinger equation with linear damping and Gaussian driving, Commun. Nonlinear Sci. Numer. Simul. **82** (2020), 105058.
- [34] G. Fotopoulos, N. I. Karachalios, V. Koukouloyannis and K. Vetas, *The linearly damped nonlinear Schrödinger equation with localized driving: spatiotemporal decay estimates and the emergence of extreme wave events*, Z. Angew. Math. Phys. **71**:3 (2020), 1–23.
- [35] N. I. Karachalios, P. Kyriazopoulos and K. Vetas, *Excitation of Peregrine-type waveforms from vanishing initial conditions in the presence of periodic forcing*, Z. Naturforsch. **A 75** (2019), 371–382.
- [36] Z. A. Anastassi, G. Fotopoulos, D. J. Frantzeskakis, T. P. Horikis, N. I. Karachalios and P. G. Kevrekidis, *Spatiotemporal algebraically localized waveforms for a nonlinear Schrödinger model with gain and loss*, Phys. D **355** (2017), 24–33.
- [37] J. M. Soto-Crespo, N. Devine and N. Akhmediev, *Integrable Turbulence and Rogue Waves: Breathers or Solitons?*, Phys. Rev. Lett. **116** (2016), 103901.
- [38] B. M. Herbst and M. J. Ablowitz, *Numerically induced chaos in the nonlinear Schrödinger equation*, Phys. Rev. Lett. **62** (1989), 2065–2068.
- [39] M. J. Ablowitz and B. M. Herbst, *On homoclinic structure and numerically induced chaos for the nonlinear Schrödinger equation*, SIAM J. Appl. Math. **50** (1990), 339–351.
- [40] J. M. Ghidaglia, *Finite dimensional behavior for the weakly damped driven Schrödinger equations*, Ann. Inst. Henri Poincaré **5** (1988), 365–405.
- [41] O. Goubet, *Regularity of the attractor for the weakly damped nonlinear Schrödinger equations*, Appl. Anal. **60** (1996), 99–119.
- [42] O. Goubet, *Regularity of the Attractor for Schrödinger Equation*, Appl. Math. Lett. **10** (1997), 57–59.
- [43] V. Achilleos, S. Diamantidis, D. J. Frantzeskakis, T. P. Horikis, N. I. Karachalios and P. G. Kevrekidis, *Collapse for the higher-order nonlinear Schrödinger equation*, Phys. D **316** (2016), 57–68.
- [44] J. M. Ball, *Global attractors for damped semilinear wave equations*, Discrete Contin. Dyn. Syst. Series **A 10** (2004), 31–52.
- [45] X. Wang, *An energy equation for the weakly damped driven nonlinear Schrödinger equations and its application to their attractors*, Phys. D **88** (1995), 167–175.
- [46] I. V. Barashenkov and Y. S. Smirnov, *Existence and stability chart for the ac-driven, damped nonlinear Schrödinger solitons*, Phys. Rev. E **54** (1996), 5707.
- [47] D. Zwillinger, *Standard Mathematical Tables and Formulae*, Chapman & Hall/CRC, 2003.